12-2011

Transverse Waves in Simulated Liquid Rocket Engines with Arbitrary Headwall Injection

Charles Toufic Haddad
chaddad1@utk.edu

To the Graduate Council:

I am submitting herewith a thesis written by Charles Toufic Haddad entitled "Transverse Waves in Simulated Liquid Rocket Engines with Arbitrary Headwall Injection." I have examined the final electronic copy of this thesis for form and content and recommend that it be accepted in partial fulfillment of the requirements for the degree of Master of Science, with a major in Aerospace Engineering.

Joseph Majdalani, Major Professor

We have read this thesis and recommend its acceptance:

Trevor Moeller, Christian Parigger

Accepted for the Council:
Carolyn R. Hodges

Vice Provost and Dean of the Graduate School

(Original signatures are on file with official student records.)

Transverse Waves in Simulated Liquid Rocket Engines with Arbitrary Headwall Injection

A Thesis Presented for the

Master of Science

Degree

The University of Tennessee, Knoxville

Charles Toufic Haddad

December 2011

Dedication

I dedicate my thesis to my loving family.

Toufic and Rita, thank you for all the guidance and support.

You are my role models and inspiration.

I wish you health and happiness.

Theodor, thank you for all the good times that we had.

You are the best brother one could wish for.

I wish you success and happiness.

Acknowledgements

First and foremost, I would like to recognize Dr. Joseph Majdalani for his assistance and mentorship that were invaluable to the completion of this project. I cherish our achievements over the past year and a half and am looking forward for a continued friendship.

Second, I would like to recognize Dr. Trevor Moeller for his guidance throughout my journey towards the Master's degree. I appreciate the productive time spent in and outside the classroom.

Third, I would like to recognize Dr. Christian Parigger for his contribution to this work. Thank you to all three committee members for dedicating time to evaluate and review this thesis.

Last but not least, I would like to recognize the University of Tennessee Space Institute and the National Science Foundation for the support that allowed me to pursue my degree and complete this research.

Thank you!

Abstract

This work introduces a closed-form analytical solution for the transverse vorticoacoustic wave in a circular cylinder with arbitrary headwall injection. This particular configuration mimics the conditions leading to the onset of traveling radial and tangential waves in a simple liquid rocket engine (LRE). Assuming a short cylindrical chamber with an injecting headwall, regular perturbations are used to linearize the problem's mass, momentum, energy, ideal gas and isentropic relations. A Helmholtz decomposition is subsequently applied to the first-order disturbance equations, thus giving rise to a compressible, inviscid and acoustic set that is responsible for driving the unsteady motion and to an incompressible, viscous and vortical set that is driven by virtue of coupling with the acoustic mode along solid boundaries. While the acoustic mode is readily recovered from the wave equation entailed in this analysis, the induced vortical mode is resolved using boundary layer theory and a judicious expansion of the rotational set with respect to a small viscous parameter, δ [delta]. After some effort, an explicit generalized formulation is presented and validated through the use of two previously investigated cases, the uniform and bell-shaped injection profiles. The solution is then extended to two new scenarios corresponding to laminar and turbulent profiles, and the results of all four settings are compared and analyzed. Moreover, the characteristics of the vorticoacoustic wave, such as penetration depth, spatial wavelength and overshoot factor, are determined. All three characteristics are found to depend on the penetration and Strouhal numbers along with the distance from the centerline. At the chamber's centerline, the waves corresponding to different injection profiles behave exactly the same and behavioral deviations are noticeable near the sidewalls.

Table of Contents

List of Tables

List of Figures

Nomenclature

a_0	=	speed of sound of incoming flow, $(\gamma R T_0)^{1/2}$
$\boldsymbol{e}_r, \boldsymbol{e}_\theta, \boldsymbol{e}_z$	=	unit vectors in r, θ, and z directions
L	=	chamber length
M_b	=	average blowing/burning Mach number at headwall
OF	=	overshoot factor
p	=	pressure
Pr	=	Prandtl number, ratio of kinematic viscosity to thermal diffusivity
r, θ, z	=	radial, tangential, and axial coordinates
R	=	chamber radius
Re_a	=	acoustic Reynolds number, $(a_0 R)/\nu_0$
Re_h	=	headwall Reynolds number, $(U_h R)/\nu_0$
S	=	Strouhal number, $k_{mn}/M_b = (\omega_0 R)/U_h$
S_p	=	effective penetration number
t	=	time
T	=	temperature
$\boldsymbol{u}$	=	total velocity vector
$U_h(r)$	=	headwall velocity profile
$\boldsymbol{U}$	=	mean flow velocity vector
V_w	=	propagation velocity of vortical waves in the axial direction
y_p	=	penetration depth of rotational elements in the y direction
z_p	=	penetration depth of rotational elements in the z direction
z_{OS}	=	locus of unsteady velocity overshoot

Greek

δ	=	viscous parameter, $\sqrt{1/Re_a}$
δ_d	=	dilatational parameter, $\delta\sqrt{\eta_0/\mu_0 + 4/3}$
ε	=	wave amplitude
γ	=	ratio of specific heats
η	=	second coefficient of viscosity, $\mu_{\text{bulk}} - 2\mu/3$
λ	=	spatial wave length
μ	=	dynamic viscosity
μ_{bulk}	=	bulk viscosity
ν	=	kinematic viscosity, μ/ρ
ρ	=	density
$\boldsymbol{\omega}$	=	unsteady vorticity
ω_0	=	non-dimensional circular frequency
$\boldsymbol{\Omega}$	=	mean vorticity

Subscripts

0	=	mean chamber properties
$r,\ \theta,\ z$	=	radial, tangential, and axial variable

Superscripts

*	=	dimensional variables
$'$	=	unsteady flow variable
$\bar{}$	=	steady flow variable
(0)	=	leading-order variable
(1)	=	first-order variable

Chapter 1

Introduction and Literature Review

Combustion instability has long been recognized as one of the most challenging problems plaguing large scale combustors. In fact, it has caused an unpredicted rise in the development costs of most rockets, leading to production delays and in some cases, the termination of many programs, such as the cancellation of the Ares V program that took place in October 2010 [1]. Combustion instabilities are considered as one of the chief obstacles in the development of rockets in general and liquid rocket engines in particular. They were observed as early as the late 1930s both in solid and liquid rocket engines and are now being observed in hybrids [2].

A. Solid Rocket Motor Instabilities

The use of solid rocket motors, or SRMs for short, dates back to 1232 AD, when the Chinese used gunpowder rockets against the Mongols who laid siege to the city of Kai-fung-fu [3]. For nearly 700 years, mankind relied exclusively on solid propellants to power its weapons. In modern rocketry, SRMs are frequently used as missiles or as strap-on boosters when a higher payload capacity is required. A major drawback in the use of SRMs is the inability to control the combustion process. Since the propellant is a mix of fuel and oxidizer, the flame cannot be extinguished once lit. In the past, this has led researchers to dedicate more time to study the instabilities in SRMs, compared to their liquid and hybrid counterparts.

The earliest analytical studies of oscillatory waves in a ducted environment with injecting walls were undertaken by Hart and McClure [4, 5], Culick [6, 7] and others [8-10]. Their models were among the few analytical solutions describing the behavior of oscillatory flows inside porous walls. Some researchers applied asymptotic approaches to linearize the Navier-Stokes equations and deduce the predicted wave behavior. Later studies [11] took into account the effects of the mean flow on wave growth and propagation in a cylinder with transpiring wall, this being the traditional geometry used to simulate a solid rocket motor.

Studies that followed emphasized the satisfaction of the no-slip boundary conditions and provided viscous and rotational corrections to the acoustic field in a solid rocket motor. On one hand, Brown, Dunlap and collaborators [12, 13] provided experimental data that confirmed the behavior of the longitudinal oscillations in the chamber. Their results showed that the models available at the time failed to satisfy the fluid's behavior next to the wall. On the other hand, Vuillot and Avalon [14] studied the growth of the sidewall boundary layer. Their analytical results predicted a thick boundary layer at the sidewall, specifically one that extended over the entire chamber volume for specific Reynolds numbers. Later analytical formulations relied on perturbation theory to provide closed-form solutions to the problem. Researchers discovered that the behavior of the oscillatory flow and its propagation into a rocket chamber depended heavily on the mean flow and injection patterns [15, 16]. Using asymptotic techniques such as WKB, Majdalani and coworkers [8, 17-19] were able to identify the dependence of the rotational

boundary layer region on the penetration number, a critical parameter that combines the injection Reynolds and Strouhal numbers in a non-intuitive way (Re / S^2).

Since the behavior of the waves is coupled with the mean flow, the proper selection of the latter is essential to establish an accurate representation of the physics at hand. In fact, early analytical investigations of the combustion instability problem may have inadvertently started with Berman [20] who, despite his interest in an entirely different industrial application, provided the means to solve for the steady state flowfield in a cylinder with injecting sidewall. Later, Yuan and Finkelstein [21] produced asymptotic solutions for the large injection and suction cases. Several studies followed, and these have mostly focused on formulating different mean flows in porous enclosures with a variety of injection configurations.

In hindsight, most of these studies have focused on the oscillatory motion within solid rocket motors. The instability affecting liquid rocket engines, albeit different in nature than that affecting SRMs, remains governed by the same laws and restrictions. Understanding longitudinal oscillations and the mathematical techniques used to quantify them leads to a better interpretation of the transverse wave behavior.

B. Liquid Rocket Engine Instabilities

On March 16, 1926 at Auburn, Massachusetts, Professor Robert H. Goddard accomplished the first recorded launch of a liquid rocket engine. The rocket, dubbed "Nell," used liquid oxygen and gasoline as propellants and maintained flight for 2.5 seconds. In World War II, German scientists and researchers developed the first long-

range missile. The V-2 LRE consumed 3,810 kg of ethanol and water and 4,910 kg of liquid oxygen to maintain flight for nearly 200 miles [22].

In modern rocketry, one of the most famous LREs is the Space Shuttle Main Engine or SSME for short. It was propelled by burning liquid hydrogen and oxygen. As in the case of large LREs, the SSME experienced acoustic oscillations that forced the designers to use Helmholtz resonators to damp out particular frequencies. To reduce instabilities, the SSME injector was designed to vaporize the propellant prior to injection. Despite the successful implementation of these measures, the main injector was still subject to wear caused by the non-destructive oscillations taking place in the chamber. Although the instabilities are attributed to acoustic oscillations, complete understanding of the mechanisms at hand is still eluding researchers. Different studies have tried to quantify their sources; these included experimental [23], numerical [24], and analytical investigations [25, 26].

In liquid rocket engines, transverse combustion instabilities are identified by large pressure oscillations, in a plane perpendicular to the axis of the combustion chamber, and corresponding frequencies that closely match linear chamber acoustics [27, 28]. Experimental observations have often suggested that the instabilities involve large amplitude oscillations with steep gradients in the direction of the flow. For instance, Clayton, Sotter and co-workers [29-31] investigated high amplitude tangential oscillations using a heavily instrumented, laboratory scale, 20 klbf thrust engine. They recorded steep-fronted pressure oscillations with peak-to-peak amplitudes one order of

magnitude larger than the mean chamber pressure. Although the response rate of their pressure transducers was not small enough to accurately capture the resulting waves, their acquired data displayed large amplitude spikes followed by long and shallow pressure segments.

Along similar lines, numerical studies have focused on the characterization of the transverse waves and their effects on combustion instability for different rocket configurations. By way of example, Ando, Inaba and Yamamoto [32] simulated the generation of transverse waves in a pulse denotation engine and deduced that the strength of the blasts increased where transverse waves collided. Other researchers, such as Chandrasekhar and Chakravarthy [33], deduced from their simulation that transverse waves could be induced by wall vibrations and, in turn, resulted in longitudinal oscillations.

In 1956, theoretical work by Maslen and Moore [34] hinted that tangential waves could not steepen as in the case of longitudinal waves. Their study on tangential wave patterns used a circular cylinder with zero mean flow. In 1962, Crocco, Harrje and Reardon [35] used small perturbations and separation of variables to predict the stability limit of liquid rocket engines. Their work showed that the stability of their rocket depended on the radial and tangential modes as well as the chamber's exit Mach number. This effort was prompted by the long-standing belief that the presence of a tangential acoustic velocity can give rise to a travelling shear wave.

C. Recent Studies

With few studies tackling the liquid rocket engine case [34-36], it was not until recently that Fischbach, Flandro and Majdalani [25] explored the transverse wave propagation in such rockets, with the purpose of understanding the mechanism of acoustic streaming. Albeit a secondary objective of theirs, they also analyzed the growth of the vorticoacoustic boundary layer at the headwall. Their configuration was somewhat analogous to the solid rocket motor case, where the sidewall takes on the role of the headwall in a liquid rocket engine.

In August 2011, Haddad and Majdalani presented an improved solution for the vorticoacoustic wave propagating in a LRE [26]. Although they provided the solution for the uniform injection profile, their research focused more on the bell-shaped profile, as the latter represented a more physical representation of the laminar mean flow. Their methodology is applied to this work and their solutions will be used as a means to validate the present generalization.

D. Scope of Work

In the present investigation, we consider the oscillatory flowfield inside a cylinder of small aspect-ratio and injecting headwall. The mean fluid motion is induced by an arbitrary injection profile. In addition to the mean flow, the presence of small-amplitude oscillatory waves is assumed. These self-excited waves give rise to a complex fluid structure that we wish to describe. Following the small perturbation approach introduced by Chu and Kovásznay [37], the equations of motion are recast into two sets: one

controlling the mean flow behavior, and the other describing the oscillatory motion. A Helmholtz decomposition is then applied to the first-order oscillatory set, thereby decomposing the latter into a pair of acoustic and vortical fields. Presently, these techniques will be used to derive an improved asymptotic solution for the oscillatory motion in a circular chamber in general, and a simulated LRE in particular. Using a systematic application of boundary layer concepts, an alternate mathematical formulation will be achieved and compared to previous work on the subject [25, 26]. At the outset, the oscillatory flow approximation based on the uniform and bell-shaped injection patterns will be shown to be a special case of the generalized solution.

Chapter 2

Problem Geometry and Headwall Injection Pattern

Modern rockets have intricate and complex chamber structures. In the LRE case, the fuel and oxidizers are pumped into the chamber using separate pumping arrangements. They are then injected through the injector faceplate whose design ensures mixing of the propellants in a minimal distance. Combustion takes place in the vicinity of the headwall and the combustion products travel down a chamber of small aspect ratio. They are then accelerated to supersonic speeds through a convergent-divergent nozzle. Figure 1 sketches the experimental setup of the $20,000$ lbf LRE used by Clayton, Rogero and Sotter [30].

A. Geometry

This work focuses on the combustion instability and wave growth taking place in the combustion chamber. Therefore, the analysis will take place in a simulated combustion chamber, where the combustion has already taken place, and the products are travelling downstream until reaching the nozzle. As shown schematically in Fig. 2, the idealized thrust chamber is simulated as a circular cylinder that extends vertically from the center axis at $r^* = 0$ to the sidewall at $r^* = R$. Horizontally, the domain extends from $z^* = 0$ to L, where the headwall may be viewed as a porous surface across which flow may be injected at a velocity $U_h(r)$. In Fig. 2, the azimuthal coordinate, θ, and the transverse direction of unsteady velocity disturbances, u'_θ and u'_r, denote both the

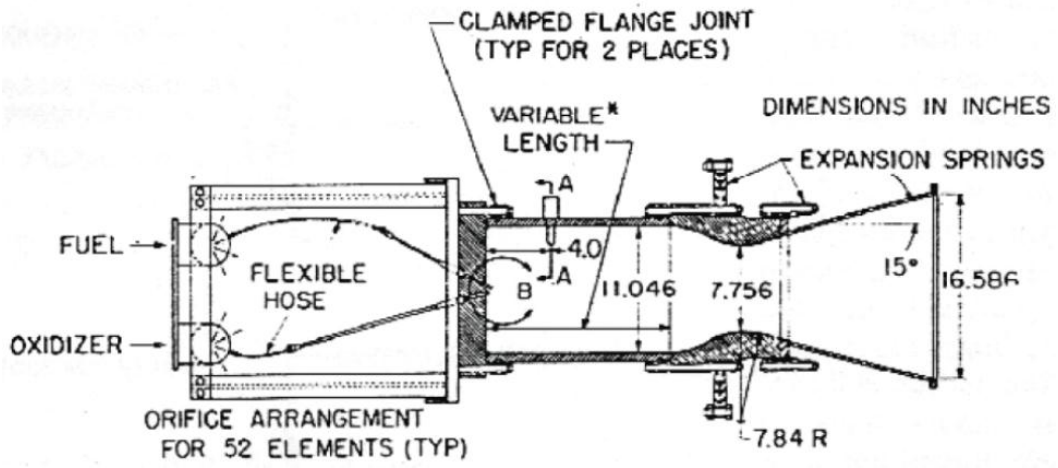

Figure 1. Schematic of an experimental setup of a LRE [30].

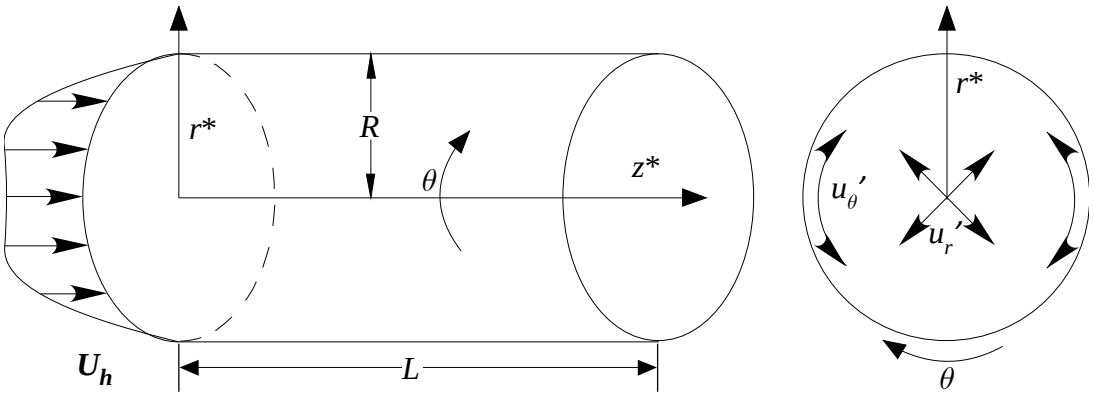

Figure 2. Chamber geometry and coordinate system showing a generally axisymmetric injection profile. Also shown is a front view depicting the couple radial and tangential wave motions that constitute the transverse modes.

tangential and radial oscillations. Given that this study is focused on a simulated LRE, the aspect ratio of the chamber under consideration is taken to be small, specifically less than or equal to unity, $L/R \leq 1$.

B. Headwall Injection Pattern

It may be instructive to note that the oscillatory behavior in the chamber is influenced by the mean flow, $\boldsymbol{U}$, the steady stream of incoming fluid across the headwall. In practice, the injection process at the faceplate can be somewhat complex, specifically when taking into account the multitude of possible injector configurations and showerhead patterns. Nonetheless, it is routinely assumed that a streamtube motion quickly develops, especially for conventional thrust chambers [38]. Bearing these factors in mind, only low-order representations of the incoming jet will be considered here.

The mathematical formulation and solution, explained in detail in Chaps. 3 and 4 respectively, are derived for an arbitrary injection profile. The general solution is then examined for four different types of injection patterns in Chap. 5. The first corresponds to a uniform, top-hat, plug flow along the chamber length. The second implements a self-similar, bell-shaped, half-cosine that is often attributed to Berman [20]. The latter has been frequently used in theoretical studies of propulsive systems with headwall injection. Examples abound and one may cite, for example: Culick [11], Brown *et al.* [12], Proudman [39], Beddini [40], Chedevergne, Casalis and Féraille [41], Griffond and Casalis [42], Saad and Majdalani [43], and Majdalani [44]. The third and fourth injection profiles are common to the fluid dynamics community and represent laminar and

turbulent velocity profiles in circular tubes [45]. The four test cases may be represented in non-dimensional form using

Uniform profile: $$\boldsymbol{U} = (0)\boldsymbol{e}_r + (0)\boldsymbol{e}_\theta + (1)\boldsymbol{e}_z \tag{2.1}$$

Berman (bell-shaped) profile: $$\boldsymbol{U} = (0)\boldsymbol{e}_r + (0)\boldsymbol{e}_\theta + \cos\left(\tfrac{1}{2}\pi r^2\right)\boldsymbol{e}_z \tag{2.2}$$

Laminar profile: $$\boldsymbol{U} = (0)\boldsymbol{e}_r + (0)\boldsymbol{e}_\theta + \left(1-r^2\right)\boldsymbol{e}_z \tag{2.3}$$

Turbulent profile: $$\boldsymbol{U} = (0)\boldsymbol{e}_r + (0)\boldsymbol{e}_\theta + \left(1-r\right)^{1/7}\boldsymbol{e}_z \tag{2.4}$$

where all velocities are normalized with respect to the centerline speed.

In what follows, the mean flow variable, $\boldsymbol{U}$, represents the arbitrary injection profile unless otherwise specified. In all four test cases, $\boldsymbol{U}$ is a sole function of the normalized radius and has no radial or tangential components. These assumptions enable the expression of Eqs. (2.1)–(2.4) in one general form

Arbitrary profile: $$\boldsymbol{U} = (0)\boldsymbol{e}_r + (0)\boldsymbol{e}_\theta + F\left(r\right)\boldsymbol{e}_z \tag{2.5}$$

where $F = F\left(r\right)$ corresponds to 1, $\cos\left(\tfrac{1}{2}\pi r^2\right)$, $1-r^2$, and $\left(1-r\right)^{1/7}$ for the uniform, bell-shaped, laminar and turbulent profiles, respectively. It is worth noting that in the domain of interest, $0 \le r \le 1$, F is always positive. This observation will prove to be essential in formulating the vortical solution in Chap. 4.

Chapter 3

Mathematical Formulation

Most fluid flows in nature can be studied as Newtonian fluids. The motion of these flows is governed by the coupled and nonlinear set of equations, the Navier-Stokes equations. A minimal set of equations characterizing the flow involves the conversation of mass, momentum and energy in addition to thermodynamic and isentropic relations. In the LRE case, gas products in the chamber behave as a Newtonian fluid. In this work, the fluid is homogeneous and the flow is compressible and adiabatic.

A. Normalized System of Equations

Finding a solution directly from the governing equation, such as the Navier-Stokes equations in this case, is usually case specific. The result is valid for one case and the derivation must be repeated for a different case, even if they are similar. To offset this issue, researchers tend to normalize the set of equation. The resulting solution is thus valid for all similar cases, and can be applied to all relevant problems by simply reverting to the original, dimensional variables. Therefore, it is helpful to first proceed by normalizing the flow variables according to

$$\begin{cases} p = p^* / P_0 & \boldsymbol{u} = \boldsymbol{u}^* / a_0 & r = r^* / R & T = T^* / T_0 \\ \rho = \rho^* / \rho_0 & t = t^* / (R / a_0) & z = z^* / R & \boldsymbol{\omega} = \boldsymbol{\omega}^* / (a_0 / R) \end{cases} \tag{3.1}$$

where reference properties are defined in the Nomenclature. The normalized governing equations for a viscous compressible fluid, with no body forces acting on it, may be expressed as

Mass: $$\frac{\partial \rho}{\partial t} + \nabla \cdot (\rho \boldsymbol{u}) = 0 \tag{3.2}$$

Momentum: $$\rho\left[\frac{\partial \boldsymbol{u}}{\partial t} + \frac{1}{2}\nabla(\boldsymbol{u}\cdot\boldsymbol{u}) - \boldsymbol{u}\times\nabla\times\boldsymbol{u}\right] = -\frac{1}{\gamma}\nabla p - \delta^2\nabla\times(\nabla\times\boldsymbol{u}) + \delta_d^2\nabla(\nabla\cdot\boldsymbol{u}) \tag{3.3}$$

Energy: $$\rho\left(\frac{\partial T}{\partial t} + \boldsymbol{u}\cdot\nabla T\right) = \frac{\gamma-1}{\gamma}\left(\frac{\partial p}{\partial t} + \boldsymbol{u}\cdot\nabla p\right) + \frac{\delta^2}{Pr_0}\nabla^2 T \tag{3.4}$$

State: $$p = \rho T \tag{3.5}$$

where Pr is the Prandtl number, γ is the ratio of specific heats, and the viscous parameters δ and δ_d are given by

$$\delta = \sqrt{\frac{\nu_0}{a_0 R}} = \sqrt{\frac{1}{Re_a}}; \quad \delta_d = \delta\sqrt{\frac{\eta_0}{\mu_0} + \frac{4}{3}} \tag{3.6}$$

The bulk viscosity, also known as the dilatational viscosity η, is taken here at the reference conditions as η_0. It represents viscous shear associated with the volumetric-rate-of-strain, and is approximately set to zero when the fluid is incompressible according to the Stokes hypothesis.

Moreover, in the case of an isentropic process, the isentropic relation may be used instead of the energy equation to generate the temperature profile of the flow.

Isentropic relation: $$p = \rho^{\gamma} \tag{3.7}$$

B. Unsteady Disturbance Equations

Since no exact solution exists for Eqs. (3.2)–(3.5), researchers have resorted to separating the normalized flow variables in terms of a mean flow and an oscillatory component. This method is amply utilized in the literature. Known examples that

showcase its importance include the reduction of the velocity-potential equation into a simpler, more manageable form and the derivation of the 1-D acoustic wave equation [46]. Chu and Kovásznay [37] decompose the normalized flow variables viz.

$$\boldsymbol{u} = M_b \boldsymbol{U} + \boldsymbol{u}'; \quad \boldsymbol{\omega} = \bar{\boldsymbol{\Omega}} + \boldsymbol{\omega}'; \quad p = 1 + p'; \quad \rho = 1 + \rho'; \quad T = 1 + T' \tag{3.8}$$

Substituting the instantaneous variables of Eq. (3.8) into Eqs. (3.2)–(3.7) leads to two sets of equations for the steady and unsteady motions [8, 17]. The next step is to expand all unsteady variables in terms of the primary perturbation parameter, ε. Each fluctuation a' may hence be written as

$$a' = \varepsilon a^{(1)} + \varepsilon^2 a^{(2)} + \varepsilon^3 a^{(3)} + \mathcal{O}(\varepsilon^4) \tag{3.9}$$

Here a alludes to a generic flow variable, and ε denotes the ratio of the superimposed oscillatory pressure amplitude to the traditionally larger mean chamber pressure. The expanded equation terms are then separated and rearranged by orders of the perturbation parameter. These sets must be solved identically for every order of ε. Since the mean flow is imposed in this study, there is no need to solve the leading order set. Instead, the analysis is limited to the first-order equations, that can be written as:

$$\frac{\partial \rho^{(1)}}{\partial t} = -\nabla \cdot \boldsymbol{u}^{(1)} - M_b \nabla \cdot \left[\rho^{(1)} \boldsymbol{U} \right] \tag{3.10}$$

$$\frac{\partial \boldsymbol{u}^{(1)}}{\partial t} = -\frac{1}{\gamma} \nabla p^{(1)} - M_b \left\{ \nabla \left[\boldsymbol{U} \cdot \boldsymbol{u}^{(1)} \right] - \boldsymbol{U} \times \boldsymbol{\omega}^{(1)} - \boldsymbol{u}^{(1)} \times \bar{\boldsymbol{\Omega}} \right\} - \delta^2 \nabla \times \boldsymbol{\omega}^{(1)} + \delta_d^2 \nabla \left[\nabla \cdot \boldsymbol{u}^{(1)} \right] \tag{3.11}$$

$$\frac{\partial T^{(1)}}{\partial t} = -M_b \boldsymbol{U} \cdot \nabla T^{(1)} + \frac{\gamma - 1}{\gamma} \left[\frac{\partial p^{(1)}}{\partial t} + M_b \boldsymbol{U} \cdot \nabla p^{(1)} \right] + \frac{\delta^2}{Pr} \nabla^2 T^{(1)} \tag{3.12}$$

$$p^{(1)} = T^{(1)} + \rho^{(1)} \tag{3.13}$$

Equations (3.10)–(3.13) are often referred to as interaction equations in which the influence of the mean flowfield, $\boldsymbol{U}$, on the unsteady disturbances, $\boldsymbol{u}^{(1)}$, is clearly seen.

C. Flowfield Decomposition

In comparable studies leading to analytical solutions of wave motions, first-order fluctuations are invariably separated into an acoustic and a vortical field [18, 47]. On the one hand, the acoustic part produces a potential motion that is compressible, irrotational, inviscid and isentropic. On the other hand, the vortical part gives rise to an incompressible, rotational, and viscous field [16]. At the onset, the potential solution, being inviscid, proves incapable of satisfying the velocity adherence condition at solid boundaries. Both physically and mathematically, a correction is required, namely in the form of a vortical wave. The latter is generated at the boundary in such a manner as to offset the acoustic part at the wall. Using a circumflex to denote the pressure-driven potential part, and a tilde for the boundary-driven vortical component, the unsteady flow variables may be once more decomposed into:

$$\boldsymbol{u}^{(1)} = \hat{\boldsymbol{u}} + \tilde{\boldsymbol{u}}; \quad \boldsymbol{\omega}^{(1)} = \hat{\boldsymbol{\omega}} + \tilde{\boldsymbol{\omega}}; \quad p^{(1)} = \hat{p} + \tilde{p}; \quad \rho^{(1)} = \hat{\rho} + \tilde{\rho}; \quad T^{(1)} = \hat{T} + \tilde{T} \tag{3.14}$$

Substituting Eq. (3.14) into Eqs. (3.10)–(3.13) yields two independent sets of equations that remain coupled by virtue of the no-slip requirement that must be fulfilled along the headwall [18]. These are:

Acoustic set:

$$\frac{\partial \hat{\rho}}{\partial t} = -\nabla \cdot \hat{\boldsymbol{u}} - M_b \boldsymbol{U} \nabla \cdot \hat{\rho} \tag{3.15}$$

$$\frac{\partial \hat{\boldsymbol{u}}}{\partial t} = -\frac{1}{\gamma} \nabla \hat{p} - M_b \left[\nabla \left(\boldsymbol{U} \cdot \hat{\boldsymbol{u}} \right) - \hat{\boldsymbol{u}} \times \bar{\boldsymbol{\Omega}} \right] \tag{3.16}$$

$$\frac{\partial \hat{T}}{\partial t} = -M_b \boldsymbol{U} \cdot \nabla \hat{T} + \frac{\gamma - 1}{\gamma} \left(\frac{\partial \hat{p}}{\partial t} + M_b \boldsymbol{U} \cdot \nabla \hat{p} \right) \tag{3.17}$$

$$\hat{p} = \hat{T} + \hat{\rho} \tag{3.18}$$

$$\hat{p} = \gamma \hat{\rho} \tag{3.19}$$

Vortical set:

$$\nabla \cdot \tilde{\boldsymbol{u}} = 0 \tag{3.20}$$

$$\frac{\partial \tilde{\boldsymbol{u}}}{\partial t} = -\frac{1}{\gamma} \nabla \tilde{p} - M_b \left[\nabla \left(\boldsymbol{U} \cdot \tilde{\boldsymbol{u}} \right) - \boldsymbol{U} \times \tilde{\boldsymbol{\omega}} - \tilde{\boldsymbol{u}} \times \bar{\boldsymbol{\Omega}} \right] - \delta^2 \nabla \times \tilde{\boldsymbol{\omega}} + \delta_d^2 \nabla \left(\nabla \cdot \tilde{\boldsymbol{u}} \right) \tag{3.21}$$

$$\frac{\partial \tilde{T}}{\partial t} = -M_b \boldsymbol{U} \cdot \nabla \tilde{T} + \frac{\gamma - 1}{\gamma} \left(\frac{\partial \tilde{p}}{\partial t} + M_b \boldsymbol{U} \cdot \nabla \tilde{p} \right) + \frac{\delta^2}{Pr} \nabla^2 \tilde{T} \tag{3.22}$$

$$\tilde{p} = \tilde{T} + \tilde{\rho} \tag{3.23}$$

D. Boundary Conditions

The fundamental disparities between acoustic and vortical fields warrant the use of two dissimilar sets of boundary conditions. In the case of the acoustic wave, a closed boundary must be maintained, as usual, along all solid surfaces, including the injection site (i.e., at $r = 1$, $z = 0$ and $z = L / R$). In the case of the rotational wave, the no-slip condition at the headwall must be secured first and foremost, being the counterpart of the

Table 1. Boundary conditions for the acoustic and vortical fields

	Boundary		
	$r=1$	$z=0$	$z=L/R$
Acoustic field	$\mathbf{n}\cdot\nabla\hat{p}=0$	$\mathbf{n}\cdot\nabla\hat{p}=0$	$\mathbf{n}\cdot\nabla\hat{p}=0$
Vortical field	no condition imposed	$u_r'=u_\theta'=u_z'=0$	bounded

sidewall boundary in the inverted analog of an axially traveling wave within an elongated porous cylinder [18, 25]. In both geometric configurations, the velocity adherence constraint is imposed at the injecting surfaces, and these correspond to either the headwall or the sidewall of the simulated LRE and SRM, respectively. Along the non-injecting surface (sidewall), slip may be allowed in the vortical wave formulation. At the downstream end of the chamber, $z=L/R$, the vortical wave must remain bounded and, being sufficiently removed from the headwall, its rotational effects are expected to have died out. Naturally, with the attenuation of the unsteady vorticity component, the vorticoacoustic wave reduces to its potential form. A summary of the physical constraints entailed in the resulting model is given in Table 1.

Chapter 4

Acoustic Solution and Viscous Correction

This chapter describes the boundary layer approach that we follow to reduce the time-dependent vortical system into a more manageable set. The ensuing formulations are provided for arbitrary mean flow profiles. However, because the vortical field is engendered by the acoustic wave, the latter must be considered first.

A. Acoustic Formulation

Although Eqs. (3.15)–(3.19) consist of an assortment of five equations, they can be systematically reduced to a single equation that represents a modified form of the wave equation. By replacing the acoustic density by the corresponding pressure, the mass equation can be rewritten in terms of the pressure and velocity only. We get

$$\frac{1}{\gamma}\frac{\partial \hat{p}}{\partial t} = -\nabla \cdot \hat{\boldsymbol{u}} - \frac{M_b}{\gamma}\boldsymbol{U}\nabla \cdot \hat{p} \tag{4.1}$$

This form decouples the momentum equation from the energy equation. The next step is to differentiate Eq. (4.1) with respect to time and to take the divergence of the acoustic momentum equation, Eq. (3.16).

$$\frac{1}{\gamma}\frac{\partial^2 \hat{p}}{\partial t^2} = -\nabla \cdot \frac{\partial \hat{\boldsymbol{u}}}{\partial t} - \frac{M_b}{\gamma}\frac{\partial}{\partial t}\left(\boldsymbol{U}\nabla \cdot \hat{p}\right) \tag{4.2}$$

$$\nabla \cdot \frac{\partial \hat{\boldsymbol{u}}}{\partial t} = -\frac{1}{\gamma}\nabla^2 \hat{p} - M_b\left[\nabla^2\left(\boldsymbol{U}\cdot\hat{\boldsymbol{u}}\right) - \nabla\cdot\left(\hat{\boldsymbol{u}}\times\bar{\boldsymbol{\Omega}}\right)\right] \tag{4.3}$$

Subtracting the derivative of the acoustic mass conservation from the divergence of the corresponding momentum equation reveals an extended form of the wave equation [25]:

$$\frac{\partial^2 \hat{p}}{\partial t^2} = \nabla^2 \hat{p} + M_b \left[\gamma \nabla^2 \left(\boldsymbol{U} \cdot \hat{\boldsymbol{u}} \right) - \gamma \nabla \cdot \left(\hat{\boldsymbol{u}} \times \bar{\boldsymbol{\Omega}} \right) - \frac{\partial}{\partial t} \left(\boldsymbol{U} \nabla \cdot \hat{p} \right) \right] \tag{4.4}$$

Note that Eq. (4.4) incorporates the effects of the mean flow, albeit at the order of the blowing Mach number. At this juncture, it may be useful to recall that the inlet or blowing Mach number is usually smaller than unity $\left(M_b \leq 0.3 < 1 \right)$. Since classical perturbation theory requires the presence of a small perturbation parameter (smaller than unity), M_b may be used as a secondary perturbation parameter. This enables us to expand the acoustic pressure in successive powers of M_b, namely,

$$\hat{p} = \hat{p}^{(0)} + M_b \hat{p}^{(1)} + M_b^2 \hat{p}^{(2)} + \mathcal{O}(M_b{}^3) \tag{4.5}$$

Forthwith, backward substitution into Eq. (4.4) renders, at leading order,

$$\frac{\partial^2 \hat{p}^{(0)}}{\partial t^2} = \nabla^2 \hat{p}^{(0)} \tag{4.6}$$

We thus recover the classical wave equation in three dimensions. The solution of this partial differential equation (PDE) may be readily extracted using separation of variables. The leading-order acoustic pressure is separable [48], such as

$$\hat{p}^{(0)} \left(t, r, \theta, z \right) = T\left(t \right) P\left(r \right) \Theta\left(\theta \right) Z\left(z \right) \tag{4.7}$$

Substituting Eq. (4.7) into the wave equation yields

$$\frac{1}{T}\frac{\partial^2 T}{\partial t^2} = \frac{1}{rP}\frac{\partial}{\partial r}\left(r\frac{\partial P}{\partial r}\right) + \frac{1}{r^2\Theta}\frac{\partial^2 \Theta}{\partial \theta^2} + \frac{1}{Z}\frac{\partial^2 Z}{\partial z^2} \tag{4.8}$$

i. Time Component

When using separation of variables in solving PDEs, two options are in order: either every component is equated to zero, which constitutes the trivial case, or each component is equivalent to a constant and the sum of these constants is null, which provides a more general solution. The latter will be used in the subsequent steps.

Since the time and axial elements are clearly separated from the other variables, it is beneficial to begin the analysis by solving their respective ODEs. Solving for time requires that

$$\frac{\partial^2 T}{\partial t^2} = \pm k_t^2 T \tag{4.9}$$

Three solutions are possible depending on the value and sign of k_t^2. Recalling that the fluid behavior is oscillatory in nature, any non-oscillatory solution must be rejected. A zero value for k_t^2 results in a linear solution, while a positive value results in an exponential behavior, both of which must be rejected. The only form that would satisfy the physics of the problem would be

$$T(t) = c_{t1}\cos(k_t t) + c_{t2}\sin(k_t t) \tag{4.10}$$

Since the actual start time of the oscillations is unknown, a smooth start of the pressure fluctuations is chosen, i.e. the time derivative of the acoustic pressure is forced to zero.

$$\frac{\partial T}{\partial t}(0) = 0 \rightarrow c_{t2} = 0 \tag{4.11}$$

A different way of representing the solution would be to use Euler's notation, where the trigonometric functions are replaced by their exponential equivalent. Taking the real part of Euler's notation reveals the true behavior in the chamber, namely,

$$T(t) = c_t \exp(ik_t t) \tag{4.12}$$

ii. Axial Component

Similarly to the time component case, the acoustic axial constituent is expected to oscillate in a sinusoidal fashion. Following the same analysis of the previous section, the axial ODE is evaluated for negative constant values only, hence,

$$\frac{\partial^2 Z}{\partial z^2} = -k_l^2 Z \tag{4.13}$$

where the corresponding solution is of the form

$$Z(z) = c_{z1} \cos(k_l z) + c_{z2} \sin(k_l z) \tag{4.14}$$

The next step is to apply the boundary conditions listed in Table 1 at the headwall and chamber exit. At the headwall, the derivative of the acoustic pressure with respect to the axial coordinate must be set to zero. One gets

$$\frac{\partial \hat{p}^{(0)}}{\partial z}(0) = \frac{\partial Z}{\partial z}(0) = 0 \rightarrow c_{z2} = 0 \tag{4.15}$$

Similarly, at the exit, the value of the axial constant k_l can be determined by applying the corresponding boundary condition.

$$\frac{\partial \hat{p}^{(0)}}{\partial z}\left(\frac{L}{R}\right)=\frac{\partial Z}{\partial z}\left(\frac{L}{R}\right)=0\rightarrow c_{z1}k_l\sin\left(k_l\frac{L}{R}\right)=0 \tag{4.16}$$

In Eq. (4.16), the trivial solution corresponding to $c_{z1}=0$ must be rejected. The only other option would be to capture the different values of k_l that would lead to the cancellation of the sine function. Since the sine function is zero at each integer multiple of π, the axial wave number k_l is equal to

$$k_l=n_l\pi\frac{R}{L}\quad\text{where}\quad n_l\in\mathbb{N} \tag{4.17}$$

The final form of the acoustic axial pressure component can be found by replacing the values of the constants of Eqs. (4.15) and (4.17) into Eq. (4.14):

$$Z(z)=c_{z1}\cos(k_l z)=c_{z1}\cos\left(n_l\pi\frac{R}{L}z\right) \tag{4.18}$$

iii. Tangential Component

Since the temporal and axial components have been successfully separated and resolved, the tangential component in Eq. (4.8) can be isolated from the radial coordinate by substituting the identified separation constants back into Eq. (4.8):

$$-k_t^2=\frac{1}{rP}\frac{\partial}{\partial r}\left(r\frac{\partial P}{\partial r}\right)+\frac{1}{r^2\Theta}\frac{\partial^2\Theta}{\partial\theta^2}-k_z^2 \tag{4.19}$$

$$\left(k_t^2-k_z^2\right)r^2+\frac{r}{P}\frac{\partial}{\partial r}\left(r\frac{\partial P}{\partial r}\right)=-\frac{1}{\Theta}\frac{\partial^2\Theta}{\partial\theta^2}=m^2 \tag{4.20}$$

In similar fashion to the temporal and axial solutions, the sign of the tangential constant m^2 is chosen to result in a sinusoidal solution,

$$\Theta(\theta) = c_{\theta 1}\cos(m\theta) + c_{\theta 2}\sin(m\theta) \tag{4.21}$$

Equation (4.21) can be rewritten in terms of the magnitude of the tangential component and its phase shift. Since there are no restrictions on the angular position of the chamber yet, the selection of phase angle is arbitrary and can be set to zero for simplification purposes. This setting dictates that the analytical pressure oscillations always peak at $\theta = 0$. A simple rotation of the solution is enough to match any computational or experimental results. Equation (4.21) begets

$$\Theta(\theta) = c_{\theta}\cos(m\theta + \varphi) = c_{\theta}\cos(m\theta) \quad \text{where} \quad m \in \mathbb{N} \tag{4.22}$$

iv. Radial Component

The last and most intricate step in determining the acoustic pressure distribution is to solve for the radial component. The derivatives in Eq. (4.20) can be expanded into

$$r^2\frac{\partial^2 P}{\partial r^2} + r\frac{\partial P}{\partial r} + \left[\left(k_t^2 - k_z^2\right)r^2 - m^2\right]P = 0 \tag{4.23}$$

Equation (4.23) is known as a Bessel ODE, whose solution, named after German mathematician Friedrich Bessel, is the sum of Bessel functions of the first and second kind.

$$P = c_{r1}J_m(k_n r) + c_{r2}Y_m(k_n r) \tag{4.24}$$

In Eq. (4.24), k_n is the radial wave number that can be deduced from the temporal and axial number viz. $k_n^2 = k_t^2 - k_z^2$, J_m is the Bessel function of the first order and Y_m is that of the second kind. Observing the behavior of the Bessel functions at the centerline is

essential in determining the value of the integration constants. In fact, Y_m tends to infinity as the radius tends to zero, for all values of m. To make sure that the solution remains bounded, c_{r2} must be forced to zero. The radial wave number can be determined by evaluating Eq. (4.24) at the boundary:

$$\frac{\partial \hat{p}^{(0)}}{\partial r}(1) = \frac{\partial P}{\partial r}(1) = 0 \rightarrow c_{r1} k_n J'_m(k_n) = 0 \tag{4.25}$$

In Eq. (4.25) and what follows, a prime implies differentiation with respect to the radial coordinate, $\partial/\partial r$. The trivial solution corresponding to $c_{r1} = 0$ must be rejected. The only other option would be to capture the different values of k_n that would lead to the cancellation of the derivative of the Bessel function. Unlike the sinusoidal functions case, values for k_n cannot be found exactly. Moreover, k_n depends on the tangential mode number m. Since different values of m lead to diverse sets of solutions for k_n, it is only fitting to rename it k_{mn}, in accordance with previous studies [25, 26]. In practice, it is deduced numerically by solving $J'_m(k_{mn}) = 0$ and generating, in successive fashion [25], the first radial, first tangential, first radial and tangential modes, etc., according to:

$$\begin{cases} k_{01} \approx 3.831\,705\,97 & k_{10} \approx 1.841\,183\,78 & k_{11} \approx 5.331\,442\,77 \\ k_{02} \approx 7.015\,586\,67 & k_{20} \approx 3.054\,236\,93 & k_{22} \approx 9.969\,467\,82 \\ k_{12} \approx 8.536\,316\,37 & k_{21} \approx 6.706\,133\,19 & \textit{etc.} \end{cases} \tag{4.26}$$

In summary, the radial component of acoustic pressure can be deduced from Eq. (4.24) as

$$P = c_r J_m(k_{mn} r) \tag{4.27}$$

v. Leading-Order Acoustic Pressure

When applying separation of variables to a PDE, the last step constitutes of substituting back each component by its solution. Replacing Eqs. (4.12), (4.18), (4.22) and (4.27) into Eq. (4.7) leads to

$$\hat{p}^{(0)}\left(t,r,\theta,z\right)=e^{-ik_t t}J_m\left(k_{mn}r\right)\cos\left(m\theta\right)\cos\left(k_l z\right) \tag{4.28}$$

where m, n and l are positive integers that refer to the tangential, radial, and longitudinal mode numbers, respectively. In the same vein, k_t, k_{mn}, m and k_l designate the temporal, radial, tangential and axial wave numbers.

To simplify the forthcoming analysis, we note that for a short cylindrical enclosure in general, or a simulated LRE in particular, the tangential and radial oscillations tend to dominate over their longitudinal counterpart, mainly due to the short length of the chamber [25, 26]. Hence, in our effort to emphasize the contribution of the transverse modes, and given that $\cos\left(k_l z\right)$ remains close to unity for small z, the axial wave number k_l is deliberately set to zero. The leading-order acoustic pressure becomes

$$\hat{p}^{(0)}\left(t,r,\theta,z\right)=e^{-ik_{mn}t}J_m\left(k_{mn}r\right)\cos\left(m\theta\right) \tag{4.29}$$

The corresponding acoustic velocity may be deduced by integrating the momentum equation and evaluating

$$\hat{\boldsymbol{u}}^{(0)}=-\frac{1}{\gamma}\int\nabla\hat{p}^{(0)}\mathrm{d}t \tag{4.30}$$

A complete leading-order acoustic solution may hence be realized, specifically

$$\hat{p} = e^{-ik_{mn}t} J_m\left(k_{mn} r\right)\cos\left(m\theta\right) \tag{4.31}$$

$$\hat{u}_r = \frac{i}{k_{mn}\gamma} e^{-ik_{mn}t} J'_m\left(k_{mn} r\right)\cos\left(m\theta\right) \tag{4.32}$$

$$\hat{u}_\theta = \frac{i}{k_{mn}\gamma}\frac{m}{r} e^{-ik_{mn}t} J_m\left(k_{mn} r\right)\sin\left(m\theta\right) \tag{4.33}$$

$$\hat{u}_z = 0 \tag{4.34}$$

For the reader's convenience, the four parts of Fig. 3 are used to illustrate the instantaneous pressure distribution in our cylindrical chamber at four sequential mode numbers. These correspond to four zeroes of J'_m that are enumerated in Eq. (4.26). Everywhere, the pressure contours represent snapshots taken in a polar plane at $t = 0.01\ \text{s}, \forall z,$ where red and blue colors denote high and low values, respectively. It is interesting to note the evolution of the nodal lines going from a) to d), thus giving rise to double-D and alternating cross patterns that characterize the acoustic modes shapes. In a) and b), the first and second radial modes are featured along with the first tangential mode where alternating double-D contours appear either a) once or b) twice, with the second set brushing along the outer periphery. In c) and d), the second tangential configuration is depicted at the first and second radial modes. The last contour clearly captures the symmetrically alternating wave structure in both tangential and radial directions.

B. Vortical Formulation

Before proceeding with the solution of the vortical disturbance, it may be useful to clarify the origin of the driving mechanisms for the waves in question, while paying

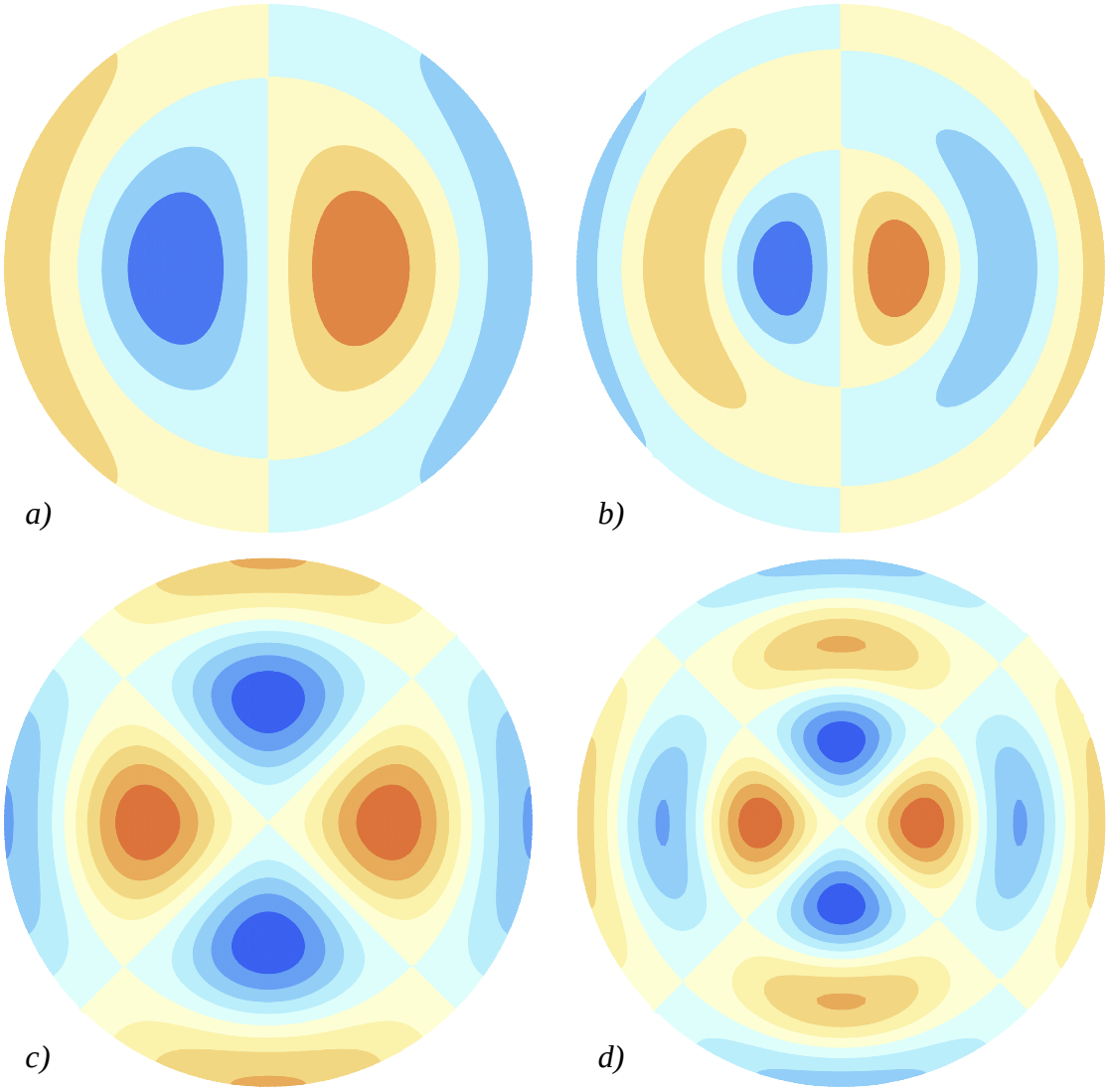

Figure 3. Pressure contours in a polar slice for transverse oscillations corresponding to : a) k_{11}, *b)* k_{12}, *c)* k_{21} *and d)* k_{22}.

special attention to the reason for the decoupling of the incompressible continuity and momentum equations from the remaining members in Eqs. (3.20)–(3.23). To this end, we recall that the acoustic wave is driven by the pressure differential in the chamber but remains uninfluenced by the no-slip requirement at the boundaries or the mean flow at the leading order in M_b. In contrast, the vortical waves are driven by the acoustic motion at the boundaries and appear only as a dissipating correction to the latter that is impacted by the chamber's geometry, the mean flow, and the acoustic field. It may hence be argued that the ensuing vortical pressure differential may be dismissed in view of the pressure differential being mainly provided by the acoustic field. This assumption enables us to ignore $\tilde{p}$ as a first approximation in the momentum equation and reduce the remaining set into [8]

$$\nabla \cdot \tilde{\boldsymbol{u}} = 0 \tag{4.35}$$

$$\frac{\partial \tilde{\boldsymbol{u}}}{\partial t} = -M_b \left[\nabla \left(\boldsymbol{U} \cdot \tilde{\boldsymbol{u}} \right) - \boldsymbol{U} \times \tilde{\boldsymbol{\omega}} - \tilde{\boldsymbol{u}} \times \bar{\boldsymbol{\Omega}} \right] - \delta^2 \nabla \times \tilde{\boldsymbol{\omega}} \tag{4.36}$$

Interestingly, the system in Eqs. (4.35)–(4.36) becomes over-determined, being comprised of four equations with three unknowns: the three velocity components, $\tilde{u}_r$, $\tilde{u}_\theta$ and $\tilde{u}_z$. A solution based on any three equations has the propensity to generate a large error in the fourth equation, depending on which three are chosen. To mathematically close the system, one can retain the small vortical pressure wave $\tilde{p}$ in the momentum equation. The amended set becomes:

$$\nabla \cdot \tilde{\boldsymbol{u}} = 0 \tag{4.37}$$

$$\frac{\partial \tilde{\boldsymbol{u}}}{\partial t} = -\frac{1}{\gamma}\nabla \tilde{p} - M_b\left[\nabla\left(\boldsymbol{U}\cdot\tilde{\boldsymbol{u}}\right) - \boldsymbol{U}\times\tilde{\boldsymbol{\omega}} - \tilde{\boldsymbol{u}}\times\bar{\boldsymbol{\Omega}}\right] - \delta^2\nabla\times\tilde{\boldsymbol{\omega}} \tag{4.38}$$

In seeking an ansatz for $\tilde{\boldsymbol{u}}$, we note that in Eqs. (4.37)–(4.38), the rotational velocity disturbance stands as a function of time and three spatial variables. Moreover, $\tilde{\boldsymbol{u}}\left(t, r, \theta, z\right)$ must be chosen in a manner to identically cancel the acoustic motion at the headwall, $\forall t$. The time dependence of the vortical field must therefore match that of the acoustic motion at the headwall. This can be achieved when the unsteady vortical wave exhibits the form:

$$\tilde{\boldsymbol{u}} = e^{-iK_{mn}t} f\left(r,\theta,z\right) \quad \text{or} \quad \frac{\partial \tilde{\boldsymbol{u}}}{\partial t} = -iK_{mn}e^{-iK_{mn}t} f\left(r,\theta,z\right) = -iK_{mn}\tilde{\boldsymbol{u}} \tag{4.39}$$

This ansatz will be later used to secure a closed-form vortical approximation.

C. Arbitrary Injection Profile

The transverse wave subject to a uniform mean flow has been briefly explored by Fischbach, Flandro and Majdalani [25] in their investigation of the acoustic streaming mechanism in a simulated LRE. A more in-depth formulation that focuses on wave characterization was later presented by Haddad and Majdalani [26] and provided detailed solutions for the uniform and bell-shaped injection profiles. The present approach applies a regular perturbation expansion to a well-established variant of the conservation equations. For the case of an arbitrary mean flow, Eqs. (4.37) and (4.38) may be expanded in scalar notation to produce

$$\frac{\tilde{u}_r}{r} + \frac{\partial \tilde{u}_r}{\partial r} + \frac{1}{r}\frac{\partial \tilde{u}_\theta}{\partial \theta} + \frac{\partial \tilde{u}_z}{\partial z} = 0 \tag{4.40}$$

$$-ik_{mn}\tilde{u}_r + M_b F\frac{\partial \tilde{u}_r}{\partial z} = -\frac{1}{\gamma}\frac{\partial \tilde{p}}{\partial r} + \delta^2\left(\frac{\partial^2 \tilde{u}_r}{\partial z^2} + \frac{1}{r^2}\frac{\partial^2 \tilde{u}_r}{\partial \theta^2} - \frac{1}{r^2}\frac{\partial \tilde{u}_\theta}{\partial \theta} - \frac{1}{r}\frac{\partial^2 \tilde{u}_\theta}{\partial r \partial \theta} - \frac{\partial^2 \tilde{u}_z}{\partial r \partial z}\right) \tag{4.41}$$

$$-ik_{mn}\tilde{u}_\theta + M_b F\frac{\partial \tilde{u}_\theta}{\partial z} = -\frac{1}{\gamma r}\frac{\partial \tilde{p}}{\partial \theta} + \delta^2\left(\frac{1}{r^2}\frac{\partial \tilde{u}_r}{\partial \theta} - \frac{1}{r}\frac{\partial^2 \tilde{u}_r}{\partial r \partial \theta} - \frac{\tilde{u}_\theta}{r^2} + \frac{\partial^2 \tilde{u}_\theta}{\partial z^2} + \frac{1}{r}\frac{\partial \tilde{u}_\theta}{\partial r} + \frac{\partial^2 \tilde{u}_\theta}{\partial r^2} - \frac{1}{r}\frac{\partial^2 \tilde{u}_z}{\partial \theta \partial z}\right) \tag{4.42}$$

$$\begin{aligned} -ik_{mn}\tilde{u}_z + M_b F\frac{\partial \tilde{u}_z}{\partial z} - M_b F'\tilde{u}_r \\ = -\frac{1}{\gamma}\frac{\partial \tilde{p}}{\partial z} + \delta^2\left(-\frac{1}{r}\frac{\partial \tilde{u}_r}{\partial z} - \frac{\partial^2 \tilde{u}_r}{\partial r \partial z} - \frac{1}{r}\frac{\partial^2 \tilde{u}_\theta}{\partial \theta \partial z} + \frac{1}{r^2}\frac{\partial^2 \tilde{u}_z}{\partial \theta^2} + \frac{1}{r}\frac{\partial \tilde{u}_z}{\partial r} + \frac{\partial^2 \tilde{u}_z}{\partial r^2}\right) \end{aligned} \tag{4.43}$$

Recognizing that the vortical wave is dominant near the boundaries, Eqs. (4.40)–(4.43) may be transformed using boundary layer theory, with the no-slip boundary condition being enforced at the headwall. Because the vortical wave can grow or decay in the axial direction, the axial variable is rescaled using a stretched inner coordinate

$$\zeta = \frac{z}{\delta} \tag{4.44}$$

The added value of the stretched axial coordinate is illustrated in Fig. 4. When using the original variable z, the near-wall boundary layer correction cannot be visibly captured. The inviscid solution seems to be valid for the entire domain, thus violating the no-slip boundary condition. However, rescaling the axial coordinate is similar to zooming in on the near wall region, which reveal the behavior of the solution. The outer inviscid solution remains adequate except in the boundary layer region where viscous forces dominate.

Being the inverted square root of the acoustic Reynolds number, the viscous parameter δ is smaller than unity and can thus be employed as a tertiary perturbation

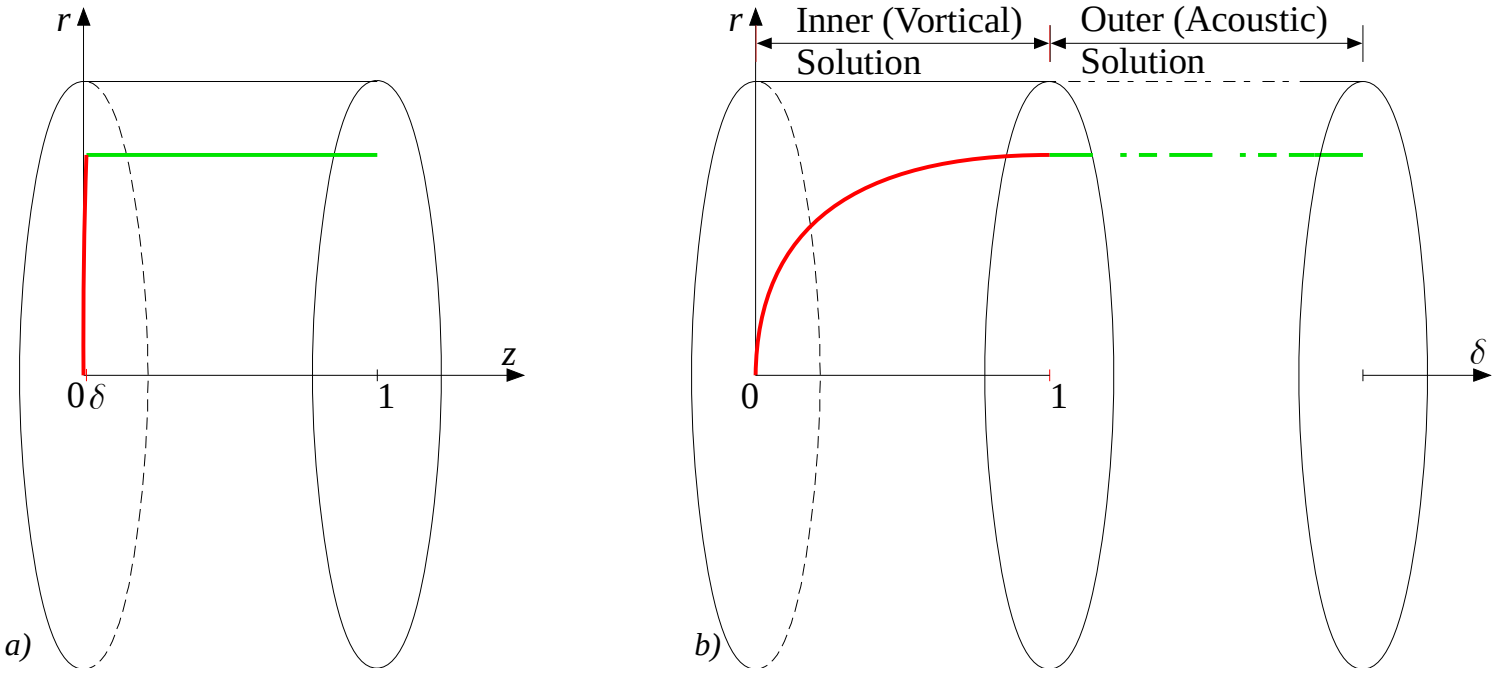

Figure 4. Chamber geometry and example of an inviscid solution and its viscous correction at the boundary for a) the unstretched axial coordinate z and b) the rescaled axial coordinate δ.

parameter. The next step is to perturb the vortical variables that appear in Eqs. (4.40)–(4.43) with respect to the viscous parameter using

$$\tilde{a} = \tilde{a}^{(0)} + \delta\tilde{a}^{(1)} + \delta^2\tilde{a}^{(2)} + \delta^3\tilde{a}^{(3)} + \mathcal{O}(\delta^4) \tag{4.45}$$

Collecting terms of the same order in δ and rearranging leads to two vortical sets that must be solved successively. When grouping terms of the same order, caution must be exercised when handling terms whose coefficient is M_b/δ. Since the Mach number and the viscous parameters are both small, their ratio is of order unity and does not affect the weight of the term.

i. Leading-Order Solution

At $\mathcal{O}(1)$, Eqs. (4.40)–(4.43) beget

$$\frac{\partial\tilde{u}_\zeta^{(0)}}{\partial\zeta} = 0 \tag{4.46}$$

$$-ik_{mn}\tilde{u}_r^{(0)} + \frac{M_b}{\delta}F\frac{\partial\tilde{u}_r^{(0)}}{\partial\zeta} - \frac{\partial^2\tilde{u}_r^{(0)}}{\partial\zeta^2} = -\frac{1}{\gamma}\frac{\partial\tilde{p}^{(0)}}{\partial r} \tag{4.47}$$

$$-ik_{mn}\tilde{u}_\theta^{(0)} + \frac{M_b}{\delta}F\frac{\partial\tilde{u}_\theta^{(0)}}{\partial\zeta} - \frac{\partial^2\tilde{u}_\theta^{(0)}}{\partial\zeta^2} = -\frac{1}{\gamma r}\frac{\partial\tilde{p}^{(0)}}{\partial\theta} \tag{4.48}$$

$$\frac{1}{\gamma}\frac{\partial\tilde{p}^{(0)}}{\partial\zeta} = 0 \tag{4.49}$$

Equations (4.46)–(4.49) are almost decoupled, with the exception of the vortical pressure term appearing on the right-hand side of the radial and tangential velocity equations. Therefore, it is beneficial to tackle Eq. (4.49) at first, keeping in mind that a simple solution would greatly simplify the vortical velocity solutions. In fact, solving Eq.

(4.49) yields an axially invariant $\tilde{p}^{(0)}$ that is only a function of the radial, tangential and time variables. Since at this order, the bulk axial propagation of the vortical wave is driven solely by the no-slip condition at the headwall, the vortical pressure does not affect the wave generated and must be set equal to zero to preserve the physicality of the case at hand.

$$\tilde{p}^{(0)} = 0 \tag{4.50}$$

Similarly, solving Eq. (4.46) leads to an axially invariant $\tilde{u}_{\zeta}^{(0)}$ that is only a function of the radial and tangential variables.

$$\tilde{u}_{\zeta}^{(0)} = G_{\zeta 0}\left(r,\theta\right) \tag{4.51}$$

At the headwall, the no-slip boundary condition must be enforced. The integration constant $G_{\zeta 0}$ is thus forced to zero, and the resulting leading-order axial vortical velocity vanishes throughout the chamber:

$$\tilde{u}_{\zeta}^{(0)} = 0 \tag{4.52}$$

Now that the $\tilde{p}^{(0)}$ has been identified, Eqs. (4.47) and (4.48) reduce to one form. The general solution of the resulting ODE is the same for both velocities. The differences emerge when applying the boundary conditions corresponding to each vortical velocity,

$$-ik_{mn}\tilde{u}_{r,\theta}^{(0)} + \frac{M_b}{\delta} F \frac{\partial \tilde{u}_{r,\theta}^{(0)}}{\partial \zeta} - \frac{\partial^2 \tilde{u}_{r,\theta}^{(0)}}{\partial \zeta^2} = 0 \tag{4.53}$$

The radial and tangential homogeneous PDE in Eq. (4.53) precipitates

$$\tilde{u}_{r,\theta}^{(0)} = A_{r,\theta}^{(0)}\left(t,r,\theta\right)e^{X_1\zeta} + B_{r,\theta}^{(0)}\left(t,r,\theta\right)e^{X_2\zeta} \tag{4.54}$$

where the axial constants X_1 and X_2 depend on the injection profile, F, and are thus functions of the radial variable, r:

$$X_1(r) = \frac{M_b}{2\delta}\left(1 - \sqrt{1 - \frac{4ik_{mn}\delta^2}{M_b^2 F^2}}\right) \tag{4.55}$$

$$X_2(r) = \frac{M_b}{2\delta}\left(1 + \sqrt{1 - \frac{4ik_{mn}\delta^2}{M_b^2 F^2}}\right) \tag{4.56}$$

At this juncture, two physical constraints may be brought to bear: the physicality of the solution in the farfield and the no-slip requirement at the headwall. First, in order to determine which of the axial constants provides a physical solution, Eqs. (4.55) and (4.56) must be rewritten in such a way to explicitly show their real and imaginary parts.:

$$X_1(r) = \frac{M_b}{2\delta}\left(1 - \sqrt{\frac{1}{2} + \frac{1}{2}\sqrt{1 + \frac{16k_{mn}^2\delta^4}{M_b^4 F^4}}} + i\sqrt{\frac{1}{2}\sqrt{1 + \frac{16k_{mn}^2\delta^4}{M_b^4 F^4}} - \frac{1}{2}}\right) \tag{4.57}$$

$$X_2(r) = \frac{M_b}{2\delta}\left(1 + \sqrt{\frac{1}{2} + \frac{1}{2}\sqrt{1 + \frac{16k_{mn}^2\delta^4}{M_b^4 F^4}}} - i\sqrt{\frac{1}{2}\sqrt{1 + \frac{16k_{mn}^2\delta^4}{M_b^4 F^4}} - \frac{1}{2}}\right) \tag{4.58}$$

As shown in Eq. (4.58), the sign of the real of X_2 depends on the injection profile F. Since F is a positive real function in the domain of interest, it does not contribute to the sign of X_2, whose positive real part would cause the vortical velocities to grow unboundedly for large ζ. Therefore, $B_{r,\theta}^{(0)}(r,\theta,t)$ must be suppressed to prevent the unphysical growth of the velocities as ζ tends to infinity. Equation (4.54) thus reduces to

$$\tilde{u}_{r,\theta}^{(0)} = A_{r,\theta}^{(0)}(t,r,\theta)e^{X_1\zeta} \tag{4.59}$$

Second, the velocity adherence condition at the headwall ($\zeta = 0$) must be satisfied for each velocity component separately, since the acoustic velocities are different. Evaluating the radial component at the headwall yields

$$\tilde{u}_r^{(0)}(t,r,\theta,0) + \hat{u}_r(t,r,\theta,0) = 0 \tag{4.60}$$

$$A_r^{(0)}(t,r,\theta) = -\frac{i}{k_{mn}\gamma} e^{-ik_{mn}t} \cos(m\theta) J_m'(k_{mn}r) \tag{4.61}$$

$$\tilde{u}_r^{(0)} = -\frac{i}{k_{mn}\gamma} e^{-ik_{mn}t} e^{X_1\zeta} \cos(m\theta) J_m'(k_{mn}r) \tag{4.62}$$

A similar procedure can be used to solve Eq. (4.59) for the tangential velocity with the outcome being

$$\tilde{u}_\theta^{(0)}(t,r,\theta,0) + \hat{u}_\theta(t,r,\theta,0) = 0 \tag{4.63}$$

$$A_\theta^{(0)}(t,r,\theta) = -\frac{i}{k_{mn}\gamma}\frac{m}{r} e^{-ik_{mn}t} J_m(k_{mn}r)\sin(m\theta) \tag{4.64}$$

$$\tilde{u}_\theta^{(0)} = -\frac{i}{k_{mn}\gamma}\frac{m}{r} e^{-ik_{mn}t} e^{X_1\zeta} \sin(m\theta) J_m(k_{mn}r) \tag{4.65}$$

The leading-order vortical solution can be summarized in the following set

$$\tilde{u}_r^{(0)} = -\frac{i}{k_{mn}\gamma} e^{-ik_{mn}t} e^{X_1\zeta} \cos(m\theta) J_m'(k_{mn}r) \tag{4.66}$$

$$\tilde{u}_\theta^{(0)} = -\frac{i}{k_{mn}\gamma}\frac{m}{r} e^{-ik_{mn}t} e^{X_1\zeta} \sin(m\theta) J_m(k_{mn}r) \tag{4.67}$$

$$\tilde{u}_\zeta^{(0)} = 0 \qquad \text{and} \qquad \tilde{p}^{(0)} = 0 \tag{4.68}$$

ii. First-Order Solution

At $\mathcal{O}(\delta)$, Eqs. (4.40)–(4.43) yield

$$\frac{\partial \tilde{u}_\zeta^{(1)}}{\partial \zeta} = -\frac{1}{r}\tilde{u}_r^{(0)} - \frac{\partial \tilde{u}_r^{(0)}}{\partial r} - \frac{1}{r}\frac{\partial \tilde{u}_\theta^{(0)}}{\partial \theta} \tag{4.69}$$

$$ik_{mn}\tilde{u}_r^{(1)} - \frac{M_b}{\delta}F\frac{\partial \tilde{u}_r^{(1)}}{\partial \zeta} + \frac{\partial^2 \tilde{u}_r^{(1)}}{\partial \zeta^2} = \frac{1}{\gamma}\frac{\partial \tilde{p}^{(1)}}{\partial r} + \frac{\partial^2 \tilde{u}_\zeta^{(0)}}{\partial r \partial \zeta} \tag{4.70}$$

$$ik_{mn}\tilde{u}_\theta^{(1)} - \frac{M_b}{\delta}F\frac{\partial \tilde{u}_\theta^{(1)}}{\partial \zeta} + \frac{\partial^2 \tilde{u}_\theta^{(1)}}{\partial \zeta^2} = -\frac{1}{\gamma r}\frac{\partial \tilde{p}^{(1)}}{\partial \theta} + \frac{1}{r}\frac{\partial^2 \tilde{u}_\zeta^{(0)}}{\partial \theta \partial \zeta} \tag{4.71}$$

$$\frac{1}{\gamma}\frac{\partial \tilde{p}^{(1)}}{\partial \zeta} = ik_{mn}\tilde{u}_\zeta{}^{(0)} - \frac{M_b}{\delta}F\frac{\partial \tilde{u}_\zeta^{(0)}}{\partial \zeta} \tag{4.72}$$

As expected from a perturbation expansion, Eqs. (4.69)–(4.72) are very similar to the leading-order equations. Their left-hand side is exactly the same as their predecessor's with the exception of being one order higher, while the right-hand side involves the zero-order contribution. The next step is to replace the known vortical velocities and pressure into Eqs. (4.69)–(4.72). The latter reduce to

$$\frac{\partial \tilde{u}_\zeta^{(1)}}{\partial \zeta} = \frac{i}{\gamma k_{mn}} e^{-ik_{mn}t}\left[k_{mn}^2 J_m\left(k_{mn}r\right)e^{X_{1C}\zeta} - \zeta e^{X_{1C}\zeta}X_1' J_m'\left(k_{mn}r\right)\right]\cos\left(m\theta\right) \tag{4.73}$$

$$ik_{mn}\tilde{u}_r^{(1)} - \frac{M_b}{\delta}F\frac{\partial \tilde{u}_r^{(1)}}{\partial \zeta} + \frac{\partial^2 \tilde{u}_r^{(1)}}{\partial \zeta^2} = \frac{1}{\gamma}\frac{\partial \tilde{p}^{(1)}}{\partial r} \tag{4.74}$$

$$ik_{mn}\tilde{u}_\theta^{(1)} - \frac{M_b}{\delta}F\frac{\partial \tilde{u}_\theta^{(1)}}{\partial \zeta} + \frac{\partial^2 \tilde{u}_\theta^{(1)}}{\partial \zeta^2} = -\frac{1}{\gamma r}\frac{\partial \tilde{p}^{(1)}}{\partial \theta} \tag{4.75}$$

$$\frac{\partial \tilde{p}^{(1)}}{\partial \zeta} = 0 \tag{4.76}$$

Following the methodology of the previous section, the first-order vortical pressure must be resolved at first, in order to simplify the solution of the corresponding velocities. Integration of Eq. (4.76) leads to an axially invariant first-order pseudo-pressure. The latter must be set to zero to preserve the physicality of the case at hand.

$$\tilde{p}^{(1)} = 0 \tag{4.77}$$

Substituting the leading-order vortical pressure by its value is Eqs. (4.74) and (4.75) leads to a homogeneous PDE whose solution is the same for the radial and tangential components,

$$ik_{mn}\tilde{u}_{r,\theta}^{(1)} - \frac{M_b}{\delta}\frac{\partial \tilde{u}_{r,\theta}^{(1)}}{\partial \zeta} + \frac{\partial^2 \tilde{u}_{r,\theta}^{(1)}}{\partial \zeta^2} = 0 \tag{4.78}$$

The solution of this homogenous PDE is analogous to that of Eq. (4.53). Similarly to the leading-order case, it has to remain bounded in the domain of interest, especially as ζ tends to infinity, namely,

$$\tilde{u}_{r,\theta}^{(1)} = A_{r,\theta}^{(1)}\left(t, r, \theta\right)e^{X_1\zeta} \tag{4.79}$$

Here too, the no-slip condition must be fulfilled. However, since the cancellation of the acoustic velocity has been accomplished at the previous order, the leading-order contribution at the headwall must not interfere. This implies

$$\tilde{u}_{r,\theta}^{(1)}\left(t, r, \theta, 0\right) = A_{r,\theta}^{(1)} = 0 \tag{4.80}$$

Equation (4.80) results in vanishing first-order radial and tangential velocities:

$$\tilde{u}_r^{(1)} = \tilde{u}_\theta^{(1)} = 0 \tag{4.81}$$

At this point, the axial component may be resolved by integrating Eq. (4.73) with respect to the stretched axial coordinate, thus leading to

$$\tilde{u}_\zeta^{(1)} = \frac{i}{\gamma k_{mn} X_1} e^{-ik_{mn}t}\left[k_{mn}^2 J_m\left(k_{mn} r\right) e^{X_1\zeta} - \left(\zeta e^{X_1\zeta} X_1 - e^{X_1\zeta}\right)\frac{X_1'}{X_1} J_m'\left(k_{mn} r\right)\right]\cos\left(m\theta\right) + A_\zeta^{(1)}\left(t,r,\theta\right) \tag{4.82}$$

Equation (4.82) must satisfy the headwall boundary condition as well. This operation involves

$$\tilde{u}_\zeta^{(1)}\left(t,r,\theta,0\right) = \frac{i}{\gamma k_{mn} X_1} e^{-ik_{mn}t}\left[k_{mn}^2 J_m\left(k_{mn} r\right) - \frac{X_1'}{X_1} J_m'\left(k_{mn} r\right)\right]\cos\left(m\theta\right) + A_\zeta^{(1)}\left(t,r,\theta\right) = 0 \tag{4.83}$$

$$A_\zeta^{(1)}\left(t,r,\theta\right) = -\frac{i}{\gamma k_{mn} X_1} e^{-ik_{mn}t}\left[k_{mn}^2 J_m\left(k_{mn} r\right) - \frac{X_1'}{X_1} J_m'\left(k_{mn} r\right)\right]\cos\left(m\theta\right) \tag{4.84}$$

The last step involves substituting the integration constant of Eq. (4.84) into Eq. (4.82). After regrouping terms, the first-order axial velocity emerges as

$$\tilde{u}_\zeta^{(1)} = \frac{i}{\gamma k_{mn} X_1} e^{-ik_{mn}t}\left[k_{mn}^2 J_m\left(k_{mn} r\right)\left(e^{X_1\zeta} - 1\right) - \left(\zeta e^{X_1\zeta} X_1 + 1 - e^{X_1\zeta}\right)\frac{X_1'}{X_1} J_m'\left(k_{mn} r\right)\right]\cos\left(m\theta\right) \tag{4.85}$$

where X_1' is the derivative with respect to r of the axial parameter and is heavily dependent on the injection profile $F\left(r\right)$, viz.

$$X_1' = \frac{\partial X_1}{\partial r} = -\frac{\delta}{M_b}\frac{2ik_{mn} r F'}{F^3\sqrt{1 - \dfrac{4iK_{mn}\delta^2}{{M_b}^2 F^2}}} \tag{4.86}$$

Figure 5 showcases the unsteady velocity vectors in a chamber cross-section taken at $t = 0.01\,\mathrm{s}$ and an axial distance of $z = 10^{-4}$ from the headwall. The four parts correspond to the same representative cases and mode numbers used to describe the

acoustic pressure in Fig. 3. As one would expect, the rich vorticoacoustic wave structures that emerge are strongly influenced by the acoustic mode shapes. The nodal lines appear to be at either 90 or 45 degree angles with respect to the pressure, thus leading to horizontal (instead of vertical) symmetry in parts a) and b) where $m = 1,$ and straight crosses (instead of oblique crosses) in parts c) and d) where $m = 2.$ In comparison to the acoustic pressure distribution displayed in Fig. 3, the nodal lines of the vorticoacoustic waves are shifted by a phase angle of $\pi/(2m).$

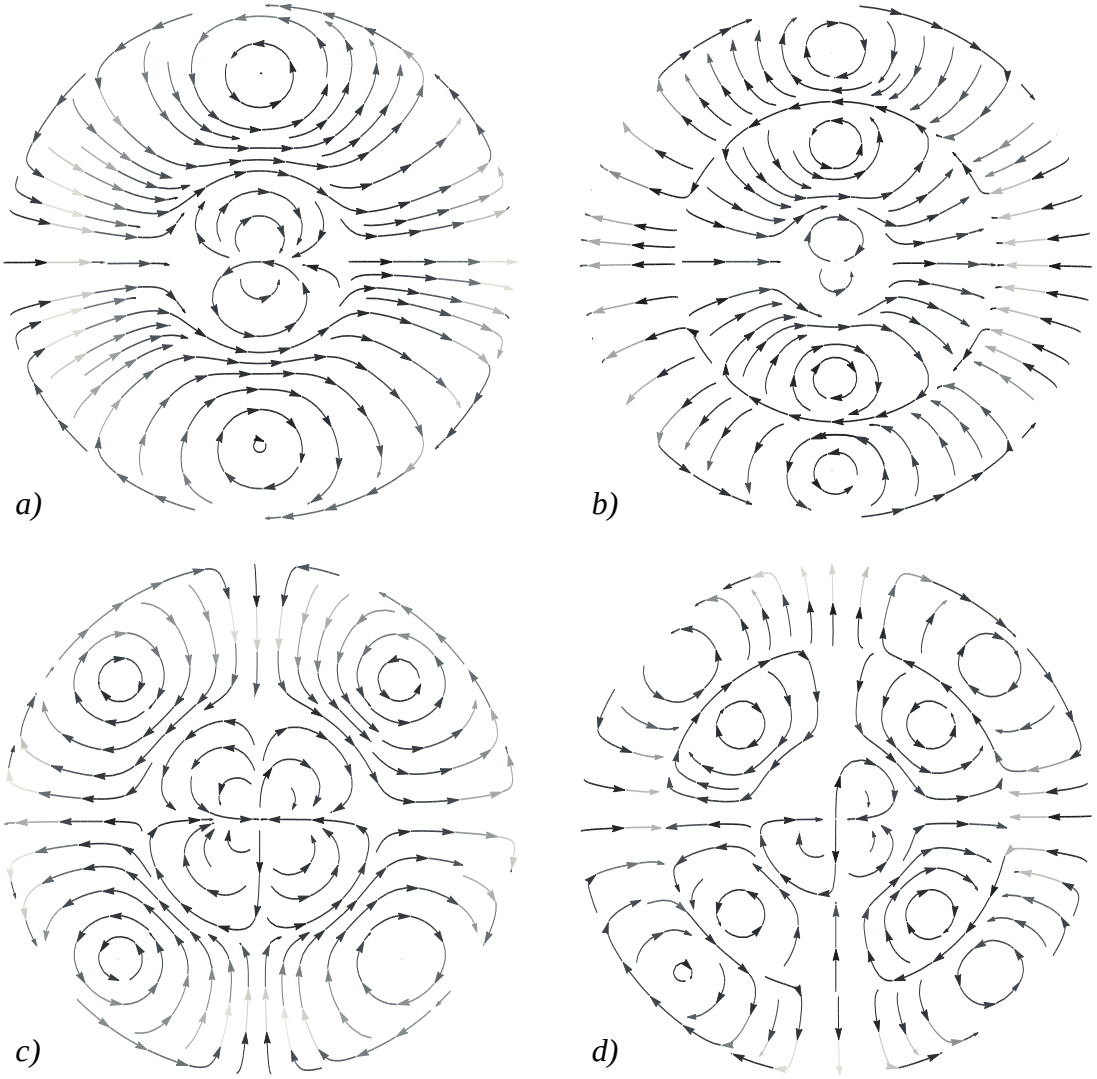

Figure 5. Vorticoacoustic velocity vectors in a polar slice, corresponding to the bell-shaped injection profile, taken at $z = 10^{-4}$ *and a transverse mode number corresponding to: a)* $k_{11} = 5.3314$, *b)* $k_{12} = 8.5363$, *c)* $k_{21} = 6.7061$ *and d)* $k_{22} = 9.9695$.

Chapter 5

Results and Discussion

The analytical approximations obtained heretofore can be collected into two sets of expressions for the vorticoacoustic velocity and pressure distributions. The significance of these results and the behavior of their corresponding waves will now be discussed. Furthermore, the wave behavior associated with each of the mean flow profiles will be compared and contrasted.

To start, a summary of the vorticoacoustic wave components is provided through the superposition of potential and rotational contributions. The resulting unsteady disturbances are given by:

$$p' = e^{-ik_{mn}t} J_m\left(k_{mn}r\right)\cos\left(m\theta\right) + \mathcal{O}(M_b, \delta^2) \tag{5.1}$$

$$u_r' = \frac{i}{k_{mn}\gamma} e^{-ik_{mn}t} J_m'\left(k_{mn}r\right)\cos\left(m\theta\right)\left(1 - e^{X_1\zeta}\right) + \mathcal{O}(M_b, \delta^2) \tag{5.2}$$

$$u_\theta' = \frac{i}{k_{mn}\gamma}\frac{m}{r} e^{-ik_{mn}t} J_m\left(k_{mn}r\right)\sin\left(m\theta\right)\left(1 - e^{X_1\zeta}\right) + \mathcal{O}(M_b, \delta^2) \tag{5.3}$$

$$u_z' = \frac{i}{k_{mn}\gamma}\frac{\delta}{X_1} e^{-ik_{mn}t}\cos\left(m\theta\right)\left[\begin{array}{l} k_{mn}^2 J_m\left(k_{mn}r\right)\left(e^{X_1\zeta} - 1\right) \\ -\dfrac{X_1'}{X_1} J_m'\left(k_{mn}r\right)\left(\zeta e^{X_1\zeta} X_1 + 1 - e^{X_1\zeta}\right) \end{array}\right] + \mathcal{O}(\delta^3) \tag{5.4}$$

A. Validation of Generalized Solution

Before proceeding to the analysis of the physical implications of the generalized solution, a validation of the results is in order. Being the subjects of past investigations [25, 26], the uniform and bell-shaped injection profiles are chosen as test cases.

The unform injection case was first investigated by Fischbach, Flandro and Majdalani [25] and then reaffirmed by Haddad and Majdalani [26]. In both studies, the vorticoacoustic waves can be expressed as

$$p' = e^{-ik_{mn}t} J_m\left(k_{mn} r\right)\cos\left(m\theta\right) + \mathcal{O}(M_b, \delta^2) \tag{5.5}$$

$$u_r' = \frac{i}{k_{mn}\gamma} e^{-ik_{mn}t} J_m'\left(k_{mn} r\right)\cos\left(m\theta\right)\left(1 - e^{X_{1U}\zeta}\right) + \mathcal{O}(M_b, \delta^2) \tag{5.6}$$

$$u_\theta' = \frac{i}{k_{mn}\gamma}\frac{m}{r} e^{-ik_{mn}t} J_m\left(k_{mn} r\right)\sin\left(m\theta\right)\left(1 - e^{X_{1U}\zeta}\right) + \mathcal{O}(M_b, \delta^2) \tag{5.7}$$

$$u_z' = \frac{ik_{mn}}{\gamma}\frac{\delta}{X_{1U}} e^{-ik_{mn}t}\cos\left(m\theta\right) J_m\left(k_{mn} r\right)\left(e^{X_{1U}\zeta} - 1\right) + \mathcal{O}(\delta^3) \tag{5.8}$$

where $X_{1U} = \dfrac{M_b}{2\delta}\left(1 - \sqrt{1 - \dfrac{4ik_{mn}\delta^2}{M_b^2}}\right)$

When comparing Eqs. (5.5)–(5.8) to Eqs. (5.1)–(5.4), three conclusions can be drawn. The vorticoacoustic pressure is the same as the acoustic pressure, which is common for all cases and is, at this order, independent of the injection profile. The vorticoacoustic radial and tangential velocities in Eqs. (5.6) and (5.7) match those of the generalized solution provided the axial constants match. In fact, X_{1U} can be recovered

from X_1, by simply substituting the injection profile F by its value of 1. The most noticeable difference is present in the expression of the axial vorticoacoustic velocity. Despite the visible dissimilarities, Eq. (5.8) is identical to Eq. (5.4) when X_1 is replaced by $X_{1\mathrm{U}}$. In fact, the constant value of $X_{1\mathrm{U}}$ leads to a vanishing $X'_{1\mathrm{U}}$, the derivative of the axial constant with respect to r, thus restoring the form derived in previous analyses.

The next step is to compare the generalized solution to that of the bell-shaped injection profile. As described by Haddad and Majdalani [26], the vorticoacoustic wave generated by the bell-shaped injection profile can be expressed as

$$p' = e^{-ik_{mn}t} J_m\left(k_{mn}r\right)\cos\left(m\theta\right) + \mathcal{O}(M_b, \delta^2) \tag{5.9}$$

$$u'_r = \frac{i}{k_{mn}\gamma} e^{-ik_{mn}t} J'_m\left(k_{mn}r\right)\cos\left(m\theta\right)\left(1 - e^{X_{1\mathrm{C}}\zeta}\right) + \mathcal{O}(M_b, \delta^2) \tag{5.10}$$

$$u'_\theta = \frac{i}{k_{mn}\gamma}\frac{m}{r} e^{-ik_{mn}t} J_m\left(k_{mn}r\right)\sin\left(m\theta\right)\left(1 - e^{X_{1\mathrm{C}}\zeta}\right) + \mathcal{O}(M_b, \delta^2) \tag{5.11}$$

$$u'_z = \frac{i}{k_{mn}\gamma}\frac{\delta}{X_{1\mathrm{C}}} e^{-ik_{mn}t}\cos\left(m\theta\right)\left[\begin{array}{l} k_{mn}^2 J_m\left(k_{mn}r\right)\left(e^{X_{1\mathrm{C}}\zeta} - 1\right) \\ -\dfrac{X'_{1\mathrm{C}}}{X_{1\mathrm{C}}} J'_m\left(k_{mn}r\right)\left(\zeta e^{X_{1\mathrm{C}}\zeta} X_{1\mathrm{C}} + 1 - e^{X_{1\mathrm{C}}\zeta}\right) \end{array}\right] + \mathcal{O}(\delta^3) \tag{5.12}$$

where $X_{1\mathrm{C}} = \dfrac{M_b}{2\delta}\left(1 - \sqrt{1 - \dfrac{4ik_{mn}\delta^2}{M_b^2\cos^2\left(\frac{1}{2}\pi r^2\right)}}\right)$

Matching Eqs. (5.9)–(5.12) to their generalized counterparts is simpler than the uniform case because the expressions are precisely similar, provided that $X_{1\mathrm{C}}$ matches

X_1 for the case at hand. In fact, the axial constants match when the injection profile F is substituted by the bell-shaped expression $\cos\left(\frac{1}{2}\pi r^2\right)$.

In addition to the uniform and bell-shaped profiles, two new cases are the subject of investigation. The classical fluid dynamics cases of laminar and turbulent profiles in a cylinder are also examined. The cases will serve as four different scenarios in the chamber. For the sake of illustration, Figs. 6, 7 and 8 are used to display the behavior of the radial, tangential and axial disturbances versus the axial coordinate at decreasing values of the inlet Mach number. In order to be consistent with previous studies, this is achieved at $t = 0$, $\delta = 0.000647$ and a thrust chamber whose aspect ratio is equal to unity ($z_{\text{exit}} = L/R = 1$) [25, 26]. Instead of plotting the waves at $r = 0.4$, $\theta = \frac{1}{3}\pi$ and k_{10} as in previous works, Figs. 6, 7 and 8 capture the oscillatory motion at $r = 1/\sqrt{2}$ and $\theta = \frac{1}{4}\pi$ for the first tangential and radial modes using k_{11}. The chosen chamber locations correspond to the radius that divides the polar slice in half and to the angle that provides equilibrium between sines and cosines for this mode number. Furthermore, the corresponding plots display the unsteady velocities at the three inlet Mach numbers of $M_b = 0.3$, $M_b = 0.03$ and $M_b = 0.003$.

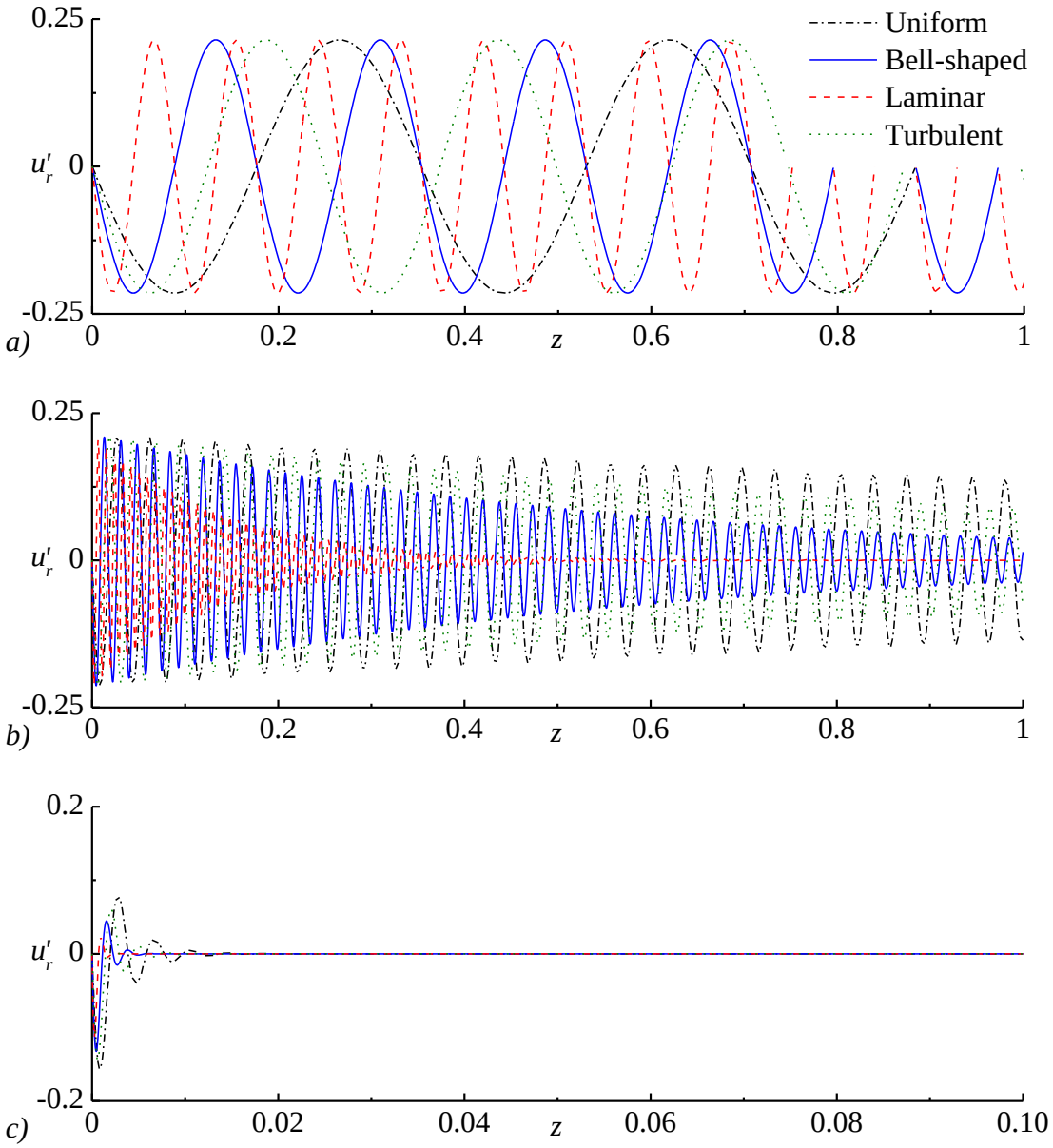

Figure 6. Unsteady radial velocity at inlet Mach numbers corresponding to: a) 0.3, b) 0.03 and c) 0.003

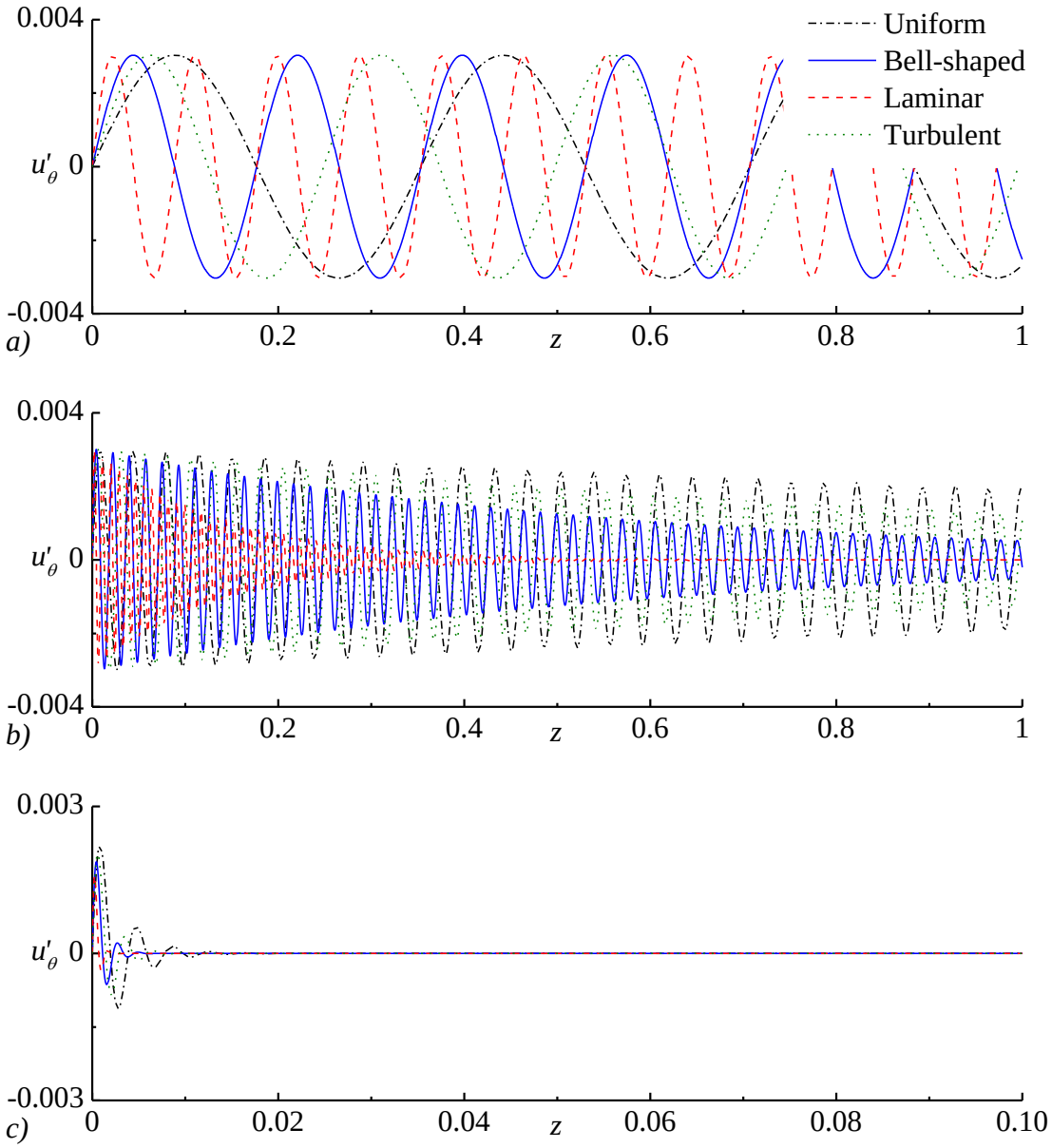

Figure 7. Unsteady tangential velocity at inlet Mach numbers corresponding to: a) 0.3, b) 0.03 and c) 0.003

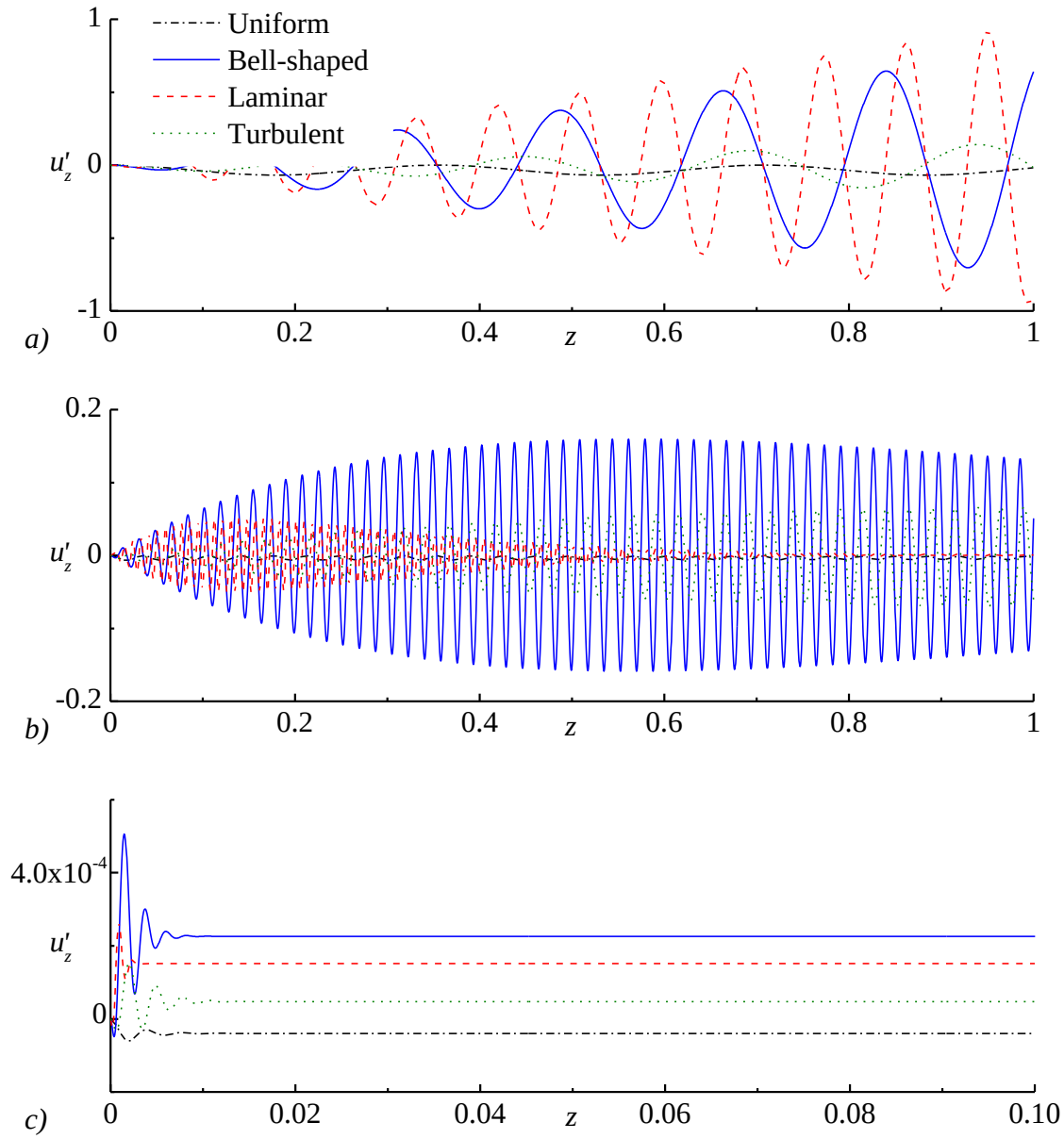

Figure 8. Unsteady axial velocity at inlet Mach numbers corresponding to: a) 0.3, b) 0.03 and c) 0.003

Table 2. Injection speeds at $r = 0.7$ for the four injection profiles.

Injection Profile	**Expression**	**Speed at $r = 0.7$**	**Rank of Speed**
Uniform	1	1	1
Bell-shaped	$\cos\left(\frac{1}{2}\pi r^2\right)$	0.7181	3
Laminar	$1-r^2$	0.51	4
Turbulent	$(1-r)^{1/7}$	0.8420	2

B. Wave Characterization

As shown in the previous section, the expressions for unsteady radial and tangential velocities in Eqs. (5.2) and (5.3) are nearly identical for all test cases. The effect of specific mean flow motion is manifested through the axial constant X_1; except for this mean flow dissimilarity, the sets in the radial and tangential directions would remain identical. The corresponding spatial distributions are hence expected to behave similarly, with minor shifts that are caused by differences in their mean flow speeds. This observation is confirmed by the plots in Figs. 6 and 7. For example, as shown in Table 2 at $r = 0.7$, the mean flow velocity is constant at unity for the uniform flow and equal to 0.7181, 0.51 and 0.8420 for the bell-shaped, laminar and turbulent profiles, respectively. Slower downstream propagation of the unsteady traveling waves can be attributed to slower injection velocities. In fact, according to Table 2, the fastest injection speed at $r = 0.7$ is the one corresponding to the uniform injection profile, followed, in order, by the turbulent, bell-shaped and laminar profiles. Correspondingly, Figs. 6 and 7

show that the associated waves are propagating downstream at speeds proportional to the injection speeds.

Interestingly, an inspection of the asymptotic orders reveals that the radial and tangential vortical velocities appear at order δ^2 (hence, of order Re_a^{-1}). This is an important observation since, in classical fluid dynamics, the normalization and subsequent analysis are traditionally based on the reciprocal of the Reynolds number, a quantity that is often taken as the primary perturbation parameter in lieu of the viscous parameter, δ. In short, it can be shown that these two velocity corrections skip every odd order and, therefore, appear only at even powers of δ. Then one may argue whether their derivation could have been achieved using the more traditional expansion, using the reciprocal of the Reynolds number. The answer is negative, owing in large part to the behavior of the axial vortical expansion. Unlike $\tilde{u}_r$ and $\tilde{u}_\theta$, the expansion of the axial vortical velocity $\tilde{u}_z$ is shifted by an order of δ from its tangential and radial counterparts, as one may infer from Eq. (5.4). This may also justify the strategy used in the present approach, including the coordinate transformation that entails stretching the axial coordinate using the viscous parameter instead of the inverse of the Reynolds number.

Concerning the vortical pseudo-pressure, it may be instructive to note that, although it was not dismissed at the onset from the rotational momentum equation, it has been carefully derived and shown to be strictly zero for the first two orders in δ. We can therefore project that the vortical wave will only affect the acoustic pressure distribution

starting at order δ^2. This observation confirms the analogous treatment of the longitudinal wave problem in a simulated SRM, where the vortical pressure is discarded throughout the analysis [8, 18]. Here, its negligible contribution is formally demonstrated.

Returning to the wave velocity, the behavior of the vortical component in the axial direction deserves particular attention. Recalling that the acoustic component of the axial wave is discounted here (assuming a short chamber), the unsteady axial wave, u_z', becomes confounded with the vortical part, $\tilde{u}_z$. The latter is needed to compensate for the more dominant tangential and radial components and, thus, ensure that continuity is fully satisfied. Figure 8 illustrates the behavior of u_z' for three injection Mach numbers. In these snapshots, the average unsteady velocity appears to be negative in the uniform injection case and positive for the bell-shaped, laminar and turbulent injection. The absolute value of the velocity is higher for the laminar and bell-shaped cases. This behavior may be attributed to the speed of the mean flow at $r = 0.7,$ where the bell-shaped and laminar patterns, in comparison to the uniform and turbulent motions, possess less energy to sustain the traveling wave motion. They are thus accompanied by faster attenuation.

To further confirm this point, an inspection of the axial constant X_1 in Eq. (4.55) shows that, at the centerline, the profile function F for the bell-shaped, laminar and turbulent cases yields a value of unity that matches the uniform flow case. Moreover, as we move away toward the sidewall, F approaches zero. In close proximity of the

sidewall, the axial constant tends to negative infinity, having a negative real part. It may therefore be seen that at the sidewall, Eqs. (5.2)–(5.4) collapse into

$$u_r' = 0 + \mathcal{O}(M_b, \delta^2) \tag{5.13}$$

$$u_\theta' = \frac{im}{k_{mn}\gamma} e^{-ik_{mn}t} J_m\left(k_{mn}\right)\sin\left(m\theta\right) + \mathcal{O}(M_b, \delta^2) \tag{5.14}$$

$$u_z' = 0 + \mathcal{O}(\delta^3) \tag{5.15}$$

Equations (5.13) and (5.15) show that through the use of a profile function that vanishes at $r = 1$ for the mean flow, the ensuing transverse wave motion can intrinsically satisfy the no-slip requirement, not only at the headwall but at the sidewall as well. This is true for the dominant component of the wave, u_r' and the axial component u_z'. As for the contribution of the tangential component u_θ', its value at the sidewall remains the same as that of the acoustic component, since the vortical contribution vanishes locally.

C. Penetration Number and Rotational Layer Thickness

Figures 6, 7 and 8 illustrate the dependence of the wave's boundary layer thickness on the injection Mach number. It is apparent that the viscous forces dominate over the inertial forces as the injection Mach number is reduced. Conversely, when the injection Mach number is increased, the boundary layer is blown off the headwall [19]. It is noted that the faster decay of the wave due to the lower Mach number results in a lower propagation wavelength, measured by the peak-to-peak distance.

Physically, the behavior of the propagation wavelength may be attributed to the wave's Strouhal number, or dimensionless frequency, defined by $S = k_{mn}/M_b$. A

decrement in the injection Mach number and its corresponding increment in the Strouhal number lead to a larger number of reversals per unit time. Furthermore, the increased frequency results in a higher interaction rate between fluid particles; the increased friction between shear layers leads to a more rapid attenuation of the wave amplitude.

Mathematically, the same behavior may be deduced by rewriting the axial decay term X_1 of Eq. (4.55) in terms of the Strouhal number and another dimensionless parameter. A two-term Maclaurin series approximation of X_1 is required to capture the amplitude (real) and oscillatory (imaginary) components. These are

$$X_1 \approx i\frac{k_{mn}\delta}{M_b F} - \frac{k_{mn}^2\delta^3}{M_b^3 F^2} = \delta\left[i\frac{S}{F} - \frac{1}{S_p F^2} \right] \tag{5.16}$$

where the effective penetration number S_p emerges in the form

$$S_p = \frac{M_b^3}{k_{mn}^2\delta^2} = \left(\frac{U_h^3}{a_0^3}\right)\left(\frac{a_0 R}{\nu_0}\right)\left(\frac{a_0^2}{\omega_0^2 R^2}\right) = \frac{U_h^3}{\nu_0\omega_0^2 R} \tag{5.17}$$

This parameter, first discovered by Majdalani [49], played a key role in the characterization of the boundary layer thickness of the longitudinal vorticoacoustic wave in a simulated solid rocket motor. Note that an increase in S_p leads to a deeper penetration of the wave. From a physical standpoint, the penetration number gauges the balance between two basic forces: unsteady inertia and viscous diffusion of the radial and tangential velocities in the axial direction. For the radial and tangential velocities, S_p may be viewed as the ratio of

$$\frac{\text{unsteady inertial force}}{\text{viscous force}} \approx \frac{\dfrac{\partial u_{r,\theta}^{*}}{\partial t^{*}}}{\nu \dfrac{\partial^2 u_{r,\theta}^{*}}{\partial z^{*2}}} \approx \frac{\dfrac{u_{r,\theta}^{*}}{t^{*}}}{\nu \dfrac{u_{r,\theta}^{*}}{z^{*2}}} = \frac{z^{*2}}{\nu t^{*}} \approx \frac{(U_h/\omega_0)^2}{\nu (R/U_b)} = \frac{U_h^3}{\nu_0 \omega_0^2 R} = S_p \tag{5.18}$$

In the present study, the wave expressions can be recast using the Strouhal and penetration numbers. The (real) magnitudes of the waves in Eqs. (5.2)–(5.4) are seen to be governed by

$$u_r' \sim J_m'\left(k_{mn} r\right)\left[1 - \exp\left(-\frac{z}{S_p F^2}\right)\right] \tag{5.19}$$

$$u_\theta' \sim J_m\left(k_{mn} r\right)\left[1 - \exp\left(-\frac{z}{S_p F^2}\right)\right] \tag{5.20}$$

$$u_z' \sim S_p F^2 \left\{ \begin{array}{l} k_{mn}^2 J_m\left(k_{mn} r\right)\left[\exp\left(-\dfrac{z}{S_p F^2}\right) - 1\right] \\ +2\dfrac{F'}{F} J_m'\left(k_{mn} r\right)\left[\dfrac{z}{S_p F^2}\exp\left(-\dfrac{z}{S_p F^2}\right) - \exp\left(-\dfrac{z}{S_p F^2}\right) + 1\right] \end{array} \right\} \tag{5.21}$$

A simple inspection of Eqs. (5.19) and (5.20) reveals that, at the sidewall, the radial component vanishes, while the tangential component scales with $J_m\left(k_{mn}\right)$; this behavior is consistent with the observations of the previous section. In contrast, two terms ensure the cancellation of the axial component of Eq. (5.21) at the sidewall. Examining the three terms in the braces reveals that the zero value of F^2 multiplying the first and last terms and the limiting value of $J_m'\left(k_{mn} r\right)/F$ as r tends to unity in the

second ensure the satisfaction of the no-slip boundary condition at the sidewall of the axial vorticoacoustic velocity.

The rotational boundary layer can also be deduced from Eqs. (5.19) and (5.20). The penetration of rotational elements is traditionally defined as the distance from the injecting boundary to the point where the contribution of the vortical wave becomes negligible, traditionally taken at 1% of the acoustic wave [19]. Since the axial component of the potential field vanishes in the farfield, the penetration depth may be deduced for the radial and tangential components by taking:

$$\exp\left(-\frac{z}{S_p F^2}\right) = \alpha = 0.01 \tag{5.22}$$

where α corresponds to 1% and z_p denotes the axial thickness of the rotational boundary layer. Rearranging Eq. (5.22) renders

$$z_p = S_p F^2 \ln(\alpha^{-1}) = \frac{M_b^3}{k_{mn}^2 \delta^2} F^2 \ln(\alpha^{-1}) \tag{5.23}$$

Figure 9 correlates the thickness of the vorticoacoustic boundary layer to the injection Mach number and viscous parameter. In conjunction with the expression in Eq. (5.23), Fig. 9 shows that the boundary layer is thick for large injection Mach numbers, exceeding by far the length of the chamber. When this case occurs, the linear oscillations have no time to decay before exiting the chamber, which would be entirely subject to transverse waves. On the other hand, in the case of a small injection Mach number, the oscillations would take their toll almost entirely in the injector zone before fading out elsewhere.

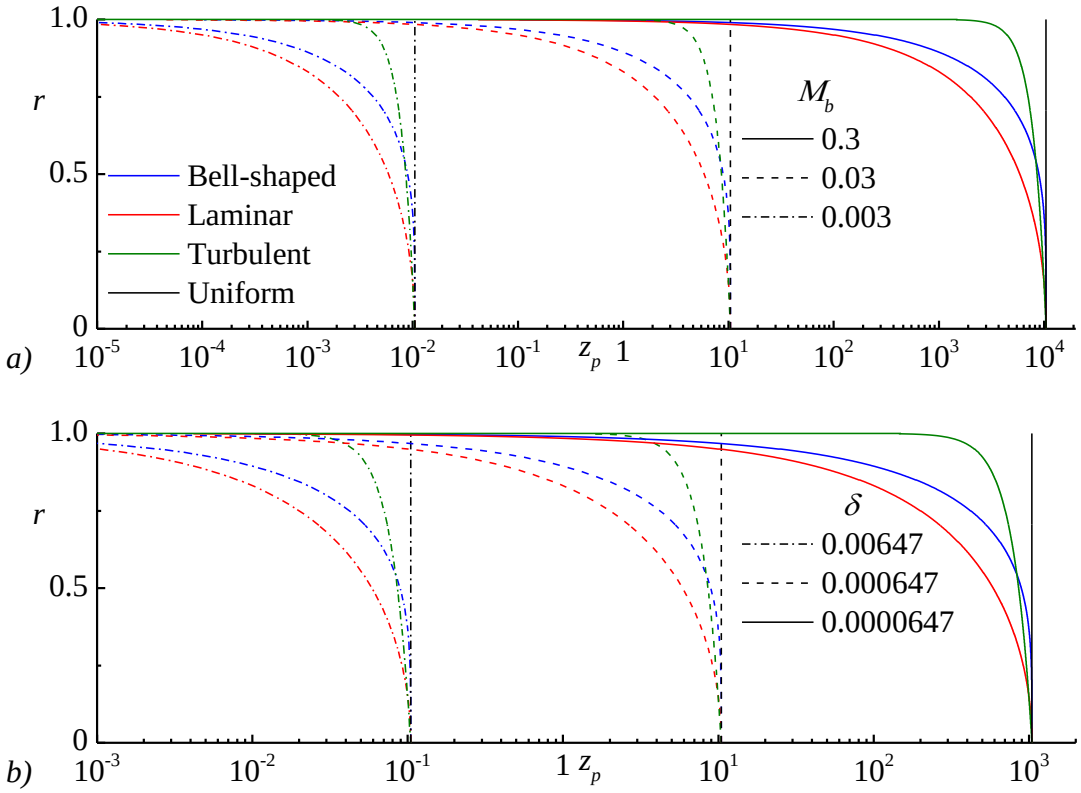

Figure 9. Different penetration depths at a) $\delta = 0.000647$ *and b)* $M_b = 0.03$ *for the bell-saped, laminar, turbulent and uniform injection profiles.*

Moreover, the dependence on the injection pattern is apparent in the expression of the penetration depth. In the bell-shaped, laminar and turbulent cases, the boundary layer thickness reaches its peak at the centerline, where disturbances are convected into the chamber at the largest headwall velocity and then depreciates precipitously to zero at the sidewall where the mean flow is forced to rest. This behavior cannot be mimicked by the uniform profile for which the penetration depth in constant throughout the chamber, a result that misrepresents the physics at hand.

Figure 10 showcases the dependence of the boundary layer's thickness on the penetration number and axial chamber position in the SRM case. Figure 11 illustrates a similar dependence in the LRE case; where the effects of the different injection mechanisms are reflected in these plots. In a solid rocket motor, particles injected radially at the sidewall must turn before merging in the longitudinal direction parallel to the chamber axis. This causes the penetration depth to increase in the direction along which

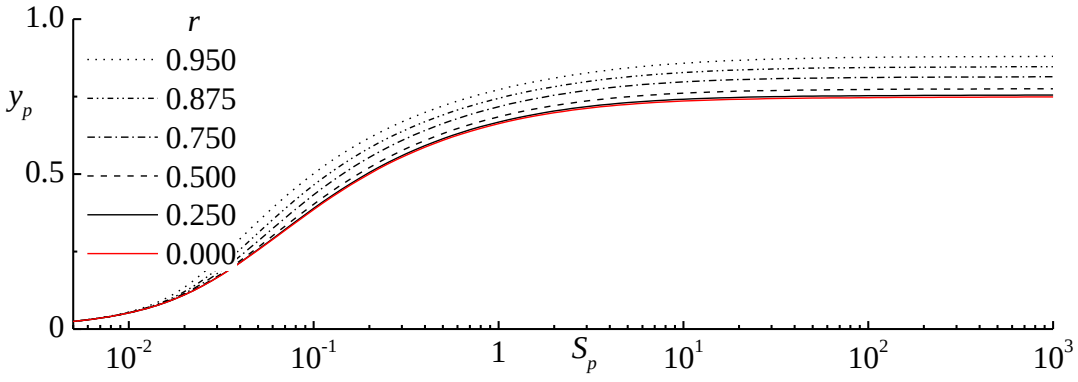

Figure 10. Penetration depth of the vortical wave corresponding to an axial configuration [19].

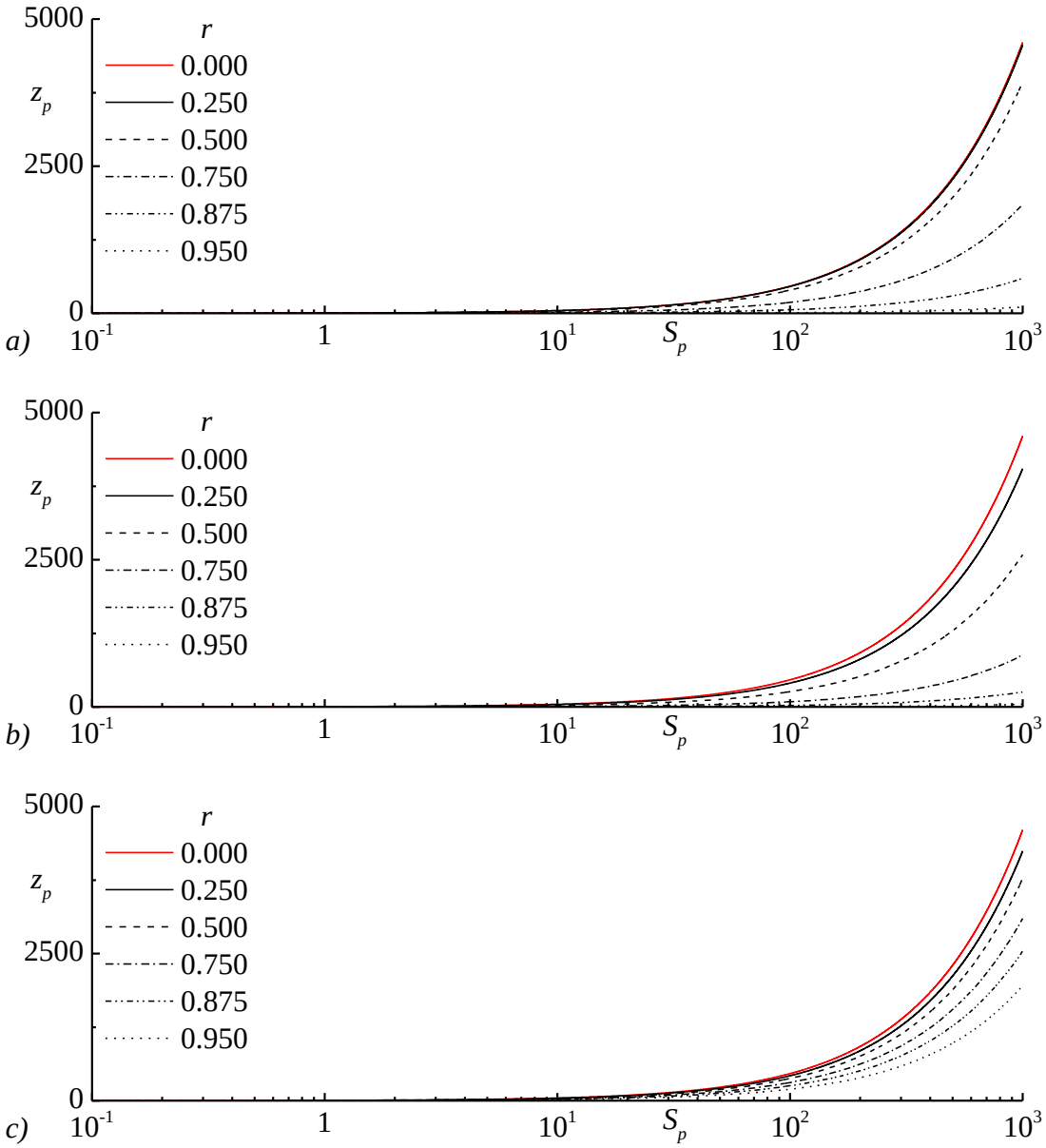

Figure 11. Penetration depth of the vortical wave corresponding to transverse configuration for the a) bell-shaped, b) laminar and c) turbulent injection profiles.

unsteady vorticity is convected by virtue of the mean flow. Conversely, in the liquid rocket engine, injection takes place at the headwall and remains unaffected by the downstream convection of unsteady vorticity. The thickness of the boundary layer is thus dependent only on the speed of injection. Throughout the chamber, a linear correlation, given by Eq. (5.23) prescribes the depth of penetration and the penetration number. Unlike the axially dominated wave problem for which the wall-normal depth of penetration y_p approaches a maximum inviscid upper limit as $S_p \to \infty$, the axial depth of penetration, z_p, will continue to grow linearly with S_p up to the point where the injection M_b would have exceeded the physical limitations of the model $\left(M_b \leq 0.3\right)$.

D. Wave Properties

In addition to the penetration depth, three properties must be investigated to complete the characterization of the vorticoacoustic wave behavior. These consist of the spatial wavelength, λ, the unsteady velocity overshoot factor, OF, and its spatial locus, z_{OS}. Since the radial and tangential components have similar expressions, the following analysis is performed using the radial component only. Nonetheless, the upcoming procedure is applicable to both waves.

i. Spatial Wavelength

The spatial wavelength, λ, defines the distance traveled by a wave during one period. It is also referred to as the distance between two consecutive peaks. To calculate λ, the wave propagation speed in the axial direction must be determined. The radial component of the vortical wave in Eq. (5.2) can be rewritten as

$$\tilde{u}_r = G(r,\theta,z)\exp\left[i\left(\frac{S}{F}z - k_{mn}t\right)\right] \tag{5.24}$$

where G represents the amplitude of the wave. With wave propagation in the axial direction being the primary concern, differentiation of the axial component is required to find the corresponding velocity. The argument of Eq. (5.24) thus yields

$$\frac{S}{F}\mathrm{d}z - k_{mn}\mathrm{d}t = 0 \tag{5.25}$$

$$V_w = \frac{\mathrm{d}z}{\mathrm{d}t} = \frac{k_{mn}F}{S} = M_b F \tag{5.26}$$

Knowing that the period of oscillation is $\tau = 2\pi/k_{mn}$, the spatial wavelength is retrieved as

$$\lambda_s = V_w\tau = \frac{F}{S} \tag{5.27}$$

Consistent with classic theory of periodic flows, the velocity of propagation is dependent only on the medium and conditions, i.e. the injection Mach number and the radial distance from the centerline. Moreover, the wavelength depends on the mode number, which is embedded in the Strouhal number. Higher modes reduce the peak-to-peak distance between oscillations, as one would expect. An important characteristic of the generalized model is the dependence of all properties on the injection profile F, which represents the radial distance from the centerline. Accordingly, oscillations in the vicinity of the sidewall propagate at a much slower rate than those located near the chamber core.

ii. Unsteady Velocity Overshoot

The presence of the Strouhal number argument in the vortical solution controls the phase difference between the strictly acoustic and vortical waves. Due to their phase difference, the two waves will periodically couple at nearly the same phase, thus resulting in an overshoot of the unsteady velocity that can reach, in some cases, twice the acoustic wave amplitude. This overshoot was first discovered by Richardson [50] who realized that maximum velocities in reciprocating flows occurred in the vicinity of the sidewall, rather than the centerline of his resonator tubes. The overshoot was later dubbed 'Richardson's annular effect.' In order to identify the location of the overshoot, Eq. (5.2) must be rewritten in term of the Strouhal and penetration numbers.

$$u_r' = G(t,r,\theta)\left[1-\exp\left(i\frac{S}{F}z\right)\exp\left(-\frac{z}{S_pF^2}\right)\right] \tag{5.28}$$

Knowing that the overshoot takes place when both waves travel in phase, this condition corresponds to $\exp\left(i\frac{S}{F}z_{\mathrm{OS}}\right)=-1$ according to Eq. (5.24); the locus of the first overshoot can thus be deduced to be

$$z_{\mathrm{OS}} = \frac{\pi F}{S} \tag{5.29}$$

Since the problem and its corresponding solution are normalized, the induced overshoot factor can be determined by combining the axial contribution of the vortical correction to that of the acoustic wave. The overshoot factor OF can be extracted from

Eq. (5.28) by evaluating the amplitude of the vorticoacoustic velocity at $z = z_{OS}$, as determined in Eq. (5.29). Starting with

$$\mathrm{OF} = 1 - \exp\left(i \frac{S}{F} z_{OS} \right) \exp\left(- \frac{z_{OS}}{S_p F^2} \right) \tag{5.30}$$

$$\mathrm{OF} = 1 - \exp\left(i\pi - \frac{\pi}{F} \frac{1}{S S_p} \right) = 1 + \exp\left(- \frac{\pi}{F} \frac{1}{S S_p} \right) \tag{5.31}$$

or

$$\mathrm{OF} = 1 + \exp\left(- \frac{\pi S}{F} \frac{\delta^2}{M_b} \right) = 1 + \exp\left(- \frac{\pi}{F} \frac{S}{Re_h} \right) \tag{5.32}$$

Figure 12 quantifies the overshoot factor and its locus for different control parameters. Note that on one hand, OF depends on the Strouhal number, the distance from the centerline and the average chamber viscosity; the latter is accounted for through the Reynolds number at the headwall, $Re_h = M_b Re_a = U_h R / \nu_0$. On the other hand, the different figures and their families of curves dramatically collapse into single lines (shown in Fig. 13a) when plotted versus the product of the Strouhal and penetration numbers. Figure 13a shows that the strength of the overshoot decreases as we move away from the chamber centerline and increases at higher values of $S S_p$, i.e. with larger injection velocities or smaller frequencies. However, the locus of the overshoot depends solely on the Strouhal number and the distance from the centerline. For all physical values of the Strouhal number, the overshoot takes place in a region smaller than 25 percent of the chamber radius in the neighborhood of the headwall.

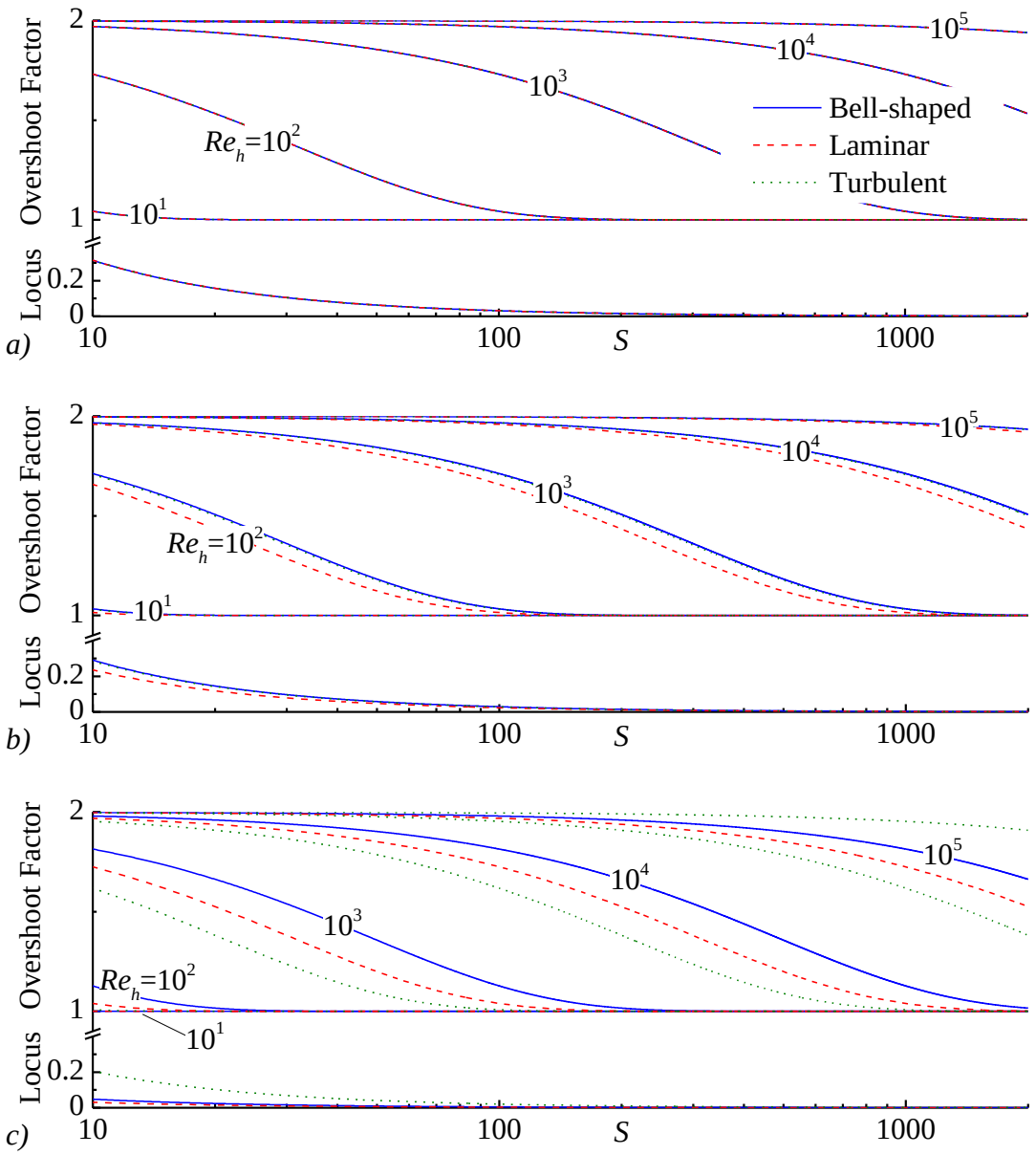

Figure 12. Overshoot factor and locus of overshoot at a) $r = 0$, *b)* $r = 0.5$ *and c)* $r = 0.95$ *for the bell-shaped, laminar and turbulent profiles.*

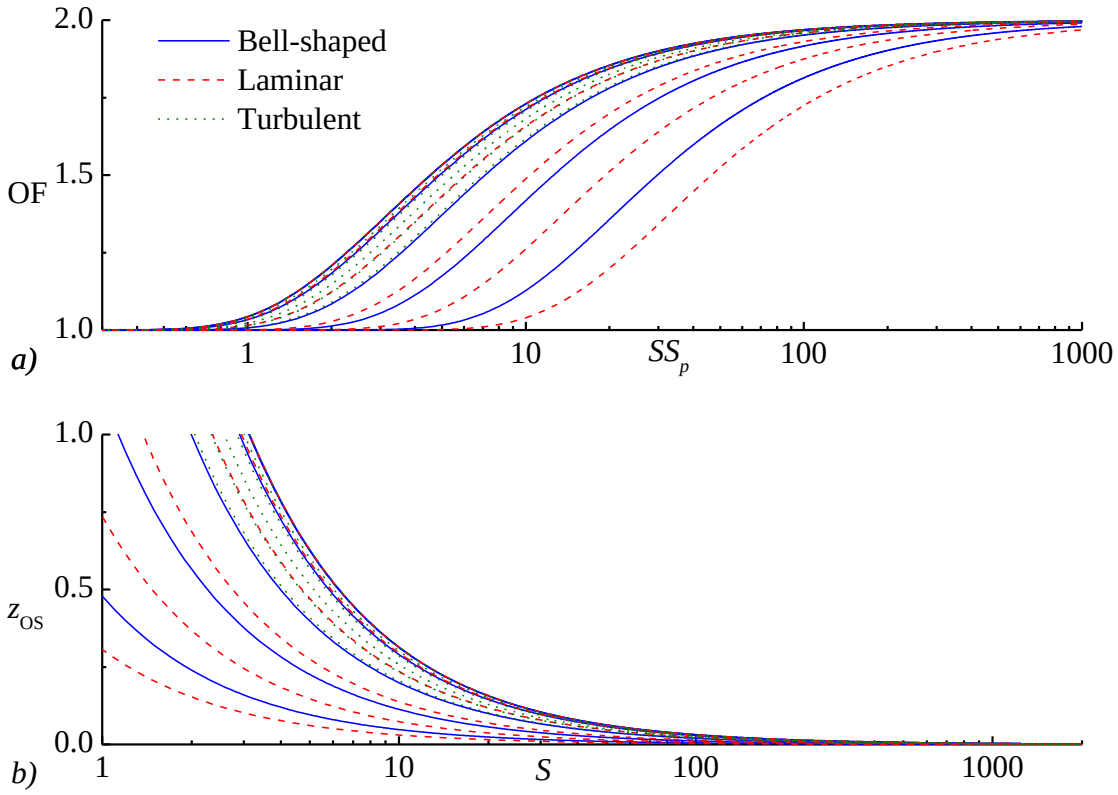

Figure 13. Effects of radial distance on a) the wave overshoot and b) its locus for the bell-shaped, laminar and turbulent cases.

Recalling that faceplate injectors protrude inwardly, they can be subject to oscillations reaching twice the strength of the predicted acoustic waves, even in the linear range. Additionally, it appears that the distance from the centerline affects the overshoot and its properties. The slower injection rate near the sidewalls leads to a smaller overshoot factor. Furthermore, as one may infer from Eq. (5.29) and Fig. 13b, z_{OS} decreases while moving away from the centerline to the extent of vanishing along the sidewall. This behavior shifts the line of maximum wave amplitude closer to the headwall as the sidewall is approached. In the case of a liquid rocket engine, these spatial excursions of peak transverse amplitudes serve to amplify shearing stresses on the injectors, where coupling between modes can lead to further steepening and shock-like behavior.

Chapter 6

Conclusions and Future Work

In this study, asymptotic expansion tools are used to capture small-to-moderate amplitude oscillations that are dominated by their transverse motion in a short circular cylinder that mimics the cold flow environment of a simple liquid rocket engine. A generalized formulation is advanced and tested for uniform, bell-shaped, laminar and turbulent injection profiles at the chamber headwall. After decomposing the unsteady wave into potential and rotational fields, the latter is resolved using a boundary layer formulation that relies on a small viscous parameter, δ. This parameter corresponds to the square root of the inverted acoustic Reynolds number based on viscosity and the speed of sound. At the outset, several fundamental flow features are unraveled including the radial, tangential, and axial velocities of the time-dependent vortical field. The pseudo-pressure associated with the rotational motion is also determined rigorously and shown to be immaterial to the present analysis.

A. Conclusions

Our generalized solution is validated by comparing the results of the previously investigated uniform [25] and bell-shaped [26] cases to those generated by this study, when applying the corresponding injection functions. The special cases are recovered exactly. The uniform injection model, however, leads to a transverse wave solution that allows slippage along the sidewall. An improved formulation is herein produced that gives rise to a more suitable representation of the oscillatory field. The latter is shown to

satisfy the no-slip boundary at both headwall and chamber sidewall for the radial and axial components. It is hoped that the mathematical strategy presented here can be later used to target higher order models of three-dimensional traveling and standing waves in various geometric settings.

Moreover, two parameters, the penetration and Strouhal numbers, are identified as controlling factors of the wave's axial propagation. The latter's dependence on these key parameters is found to be nearly identical to its counterpart arising in the longitudinal wave analog encountered in the treatment of oscillatory motion in solid rocket motors [8, 18]. The advent of these parameters enables the full characterization of the penetration depth in the direction normal to the injecting surface. With the vorticoacoustic solution at hand, fundamental wave propagation properties are carefully extracted and discussed. These include the depth of penetration and Richardson's overshoot factor of the transverse waves. These are found to be strongly dependent on the Strouhal and penetration numbers.

Lastly, the locus of peak wave amplitudes, in particular, is found to be smaller than a quarter radius, thus placing the maximum shearing stresses resulting from transverse wave motion in the close vicinity of the headwall. Despite the linear restrictions of this work, it demonstrates the combination of vortical and acoustic waves doubles the magnitude of the acoustic wave in the region of protruding injectors, for a large range of frequencies and injection Mach numbers. These observations are crucial

analytical steps in determining the wear and stresses that affect chamber components in a liquid rocket engine.

B. Future Work

In future work, the steepening of these waves should be examined, thus relaxing the linear domain restriction and allowing for an analytical formulation of the shock-like behavior of the combustion products exiting the chamber. Additional effort should be also invested in ensuring the satisfaction of all no-slip boundary conditions in the chamber. Further investigation of higher order viscous corrections and their effect on the vortical pressure must also be pursued.

List of References

1. Malik, T. President Obama Signs New Vision for U.S. Space Exploration Into Law. Space.com, 2010.
2. Culick, F.E.C., Unsteady Motions in Combustion Chambers for Propulsion Systems, 2006, North Atlantic Treaty Organization. p. 664.
3. Martin, W.A.P., The Lore of Cathay; or, The Intellect of China, 1901, New York: Fleming H. Revell Company.
4. Hart, R. and F. McClure, Combustion instability: acoustic interaction with a burning propellant surface. The Journal of Chemical Physics, 1959. **30**(6): p. 1501-1514. doi: 10.1063/1.1730226
5. Hart, R. and F. McClure, Theory of acoustic instability in solid-propellant rocket combustion. Tenth Symposium (International) on Combustion, 1965. **10**(1): p. 1047-1065. doi: 10.1016/S0082-0784(65)80246-6
6. Culick, F., High frequency oscillations in liquid rockets. AIAA Journal, 1963. **1**(5): p. 1097-1104. doi:
7. Culick, F., Acoustic oscillations in solid propellant rocket chambers. Acta Astronautica, 1966. **12**(2): p. 113-126. doi:
8. Majdalani, J. and T. Roh, The oscillatory channel flow with large wall injection. Proceedings of the Royal Society of London, Series A, 2000. **456**(1999): p. 1625-1657. doi: 10.1098/rspa.2000.0579
9. Fabignon, Y., et al., Instabilities and pressure oscillations in solid rocket motors. Journal of Aerospace Science and Technology, 2003. **7**(3): p. 191-200. doi: 10.1016/S1270-9638(02)01194-X
10. Fischbach, S., J. Majdalani, and G. Flandro, Acoustic instability of the slab rocket motor. Journal of Propulsion and Power, 2007. **23**(1): p. 146-157. doi: 10.2514/1.14794
11. Culick, F., Rotational axisymmetric mean flow and damping of acoustic waves in a solid propellant rocket. AIAA Journal, 1966. **4**(8): p. 1462-1464. doi: 10.2514/3.3709
12. Brown, R.S., A.M. Blackner, P.G. Willoughby, and R. Dunlap, Coupling between acoustic velocity oscillations and solid propellant combustion. Journal of Propulsion and Power, 1986. **2**(5): p. 428-437. doi: 10.2514/3.22925
13. Dunlap, R., et al., Internal flow field studies in a simulated cylindrical port rocket chamber. Journal of Propulsion and Power, 1990. **6**(6): p. 690-704. doi: 10.2514/3.23274

14. Vuillot, F. and G. Avalon, Acoustic boundary layers in large solid propellant rocket motors using Navier-Stokes equations. Journal of Propulsion and Power, 1991. **7**(2): p. 231-239. doi:
15. Majdalani, J. and W. Van Moorhem, Improved time-dependent flowfield solution for solid rocket motors. AIAA Journal, 1998. **36**(2): p. 241-248. doi: 10.2514/2.7507
16. Majdalani, J. and G. Flandro, The oscillatory pipe flow with arbitrary wall injection. Proceedings of the Royal Society of London, Series A, 2002. **458**(2023): p. 1621-1651. doi: 10.1098/rspa.2001.0930
17. Majdalani, J. and W. Van Moorhem, Multiple-scales solution to the acoustic boundary layer in solid rocket motors. Journal of Propulsion and Power, 1997. **13**(2): p. 186-193. doi: 10.2514/2.5168
18. Majdalani, J., Multiple asymptotic solutions for axially travelling waves in porous channels. Journal of Fluid Mechanics, 2009. **636**(1): p. 59-89. doi: 10.1017/S0022112009007939
19. Majdalani, J., The boundary layer structure in cylindrical rocket motors. AIAA Journal, 1999. **37**(4): p. 505-508. doi: 10.2514/2.742
20. Berman, A.S., Laminar flow in channels with porous walls. Journal of Applied Physics, 1953. **24**(9): p. 1232-1235. doi: 10.1063/1.1721476
21. Yuan, S. and A. Finkelstein, Laminar pipe flow with injection and suction through a porous wall. Transactions of the American Society of Mechanical Engineers: Journal of Applied Mechanics, 1956. **78**(3): p. 719-724. doi:
22. Kennedy, G.P., Vengeance Weapon 2: the V-2 Guided Missile. Vol. 9. 1983: National Air and Space Museum by the Smithsonian Institution Press.
23. Richecoeur, F., S. Ducruix, P. Scouflaire, and S. Candel, Experimental investigation of high-frequency combustion instabilities in liquid rocket engine. Acta Astronautica, 2008. **62**(1): p. 18-27. doi: 10.1016/j.actaastro.2006.12.034
24. Smith, R., et al., Computational investigation of acoustics and instabilities in a longitudinal-mode rocket combustor. AIAA Journal, 2008. **46**(11): p. 2659-2673. doi: 10.2514/1.28125

25. Fischbach, S., G. Flandro, and J. Majdalani, Acoustic streaming in simplified liquid rocket engines with transverse mode oscillations. Physics of Fluids, 2010. **22**(6): p. 063602-063621. doi: 10.1063/1.3407663
26. Haddad, C.T. and J. Majdalani. Transverse Waves in Simluated Liquid Rocket Engines. in 47th AIAA/ASME/SAE/ASEE Joint Propulsion Conference & Exhibit. 2011. San Diego.
27. Flandro, G.A., J. Majdalani, and J.D. Sims. Nonlinear longitudinal mode instability in liquid propellant rocket engine preburners. in AIAA. 2004. Tucson, AZ.
28. Flandro, G.A., J. Majdalani, and J.D. Sims. On nonlinear combustion instability in liquid propellant rocket engines. in AIAA. 2004. Tucson, AZ.
29. Clayton, R.M., Experimental Measurements on Rotating Detonation-Like Combustion, 1965, JPL: Pasadena, CA.
30. Clayton, R., R. Rogero, and J. Sotter, An experimental description of destructive liquid rocket resonant combustion. AIAA Journal, 1968. **6**(7): p. 1252-1259. doi: 10.2514/3.4730
31. Sotter, J., J. Woodward, and R. Clayton, Injector response to strong high-frequency pressure oscillations. Journal of Spacecraft and Rockets, 1969. **6**(4): p. 504-506. doi: 10.2514/3.29696
32. Maicke, B.A., T. Saad, and J. Majdalani. On the compressible Hart-McClure mean flow motion in simulated rocket motors. in AIAA. 2010. Nashville, TN.
33. Terrill, R., An exact solution for flow in a porous pipe. Zeitschrift für Angewandte Mathematik und Physik (ZAMP), 1982. **33**(4): p. 547-552. doi: 10.1007/BF00955703
34. Maslen, S. and F. Moore, On strong transverse waves without shocks in a circular cylinder. Journal of the Aeronautical Sciences, 1956. **23**(6): p. 583-593. doi:
35. Crocco, L., D. Harrje, and F. Reardon, Transverse combustion instability in liquid propellant rocket motors. J. Am. Rock. Soc, 1962. **32**: p. 366. doi:
36. Zinn, B.T. and C.T. Savell, A theoretical study of three-dimensional combustion instability in liquid-propellant rocket engines. Symposium (International) on Combustion, 1969. **12**(1): p. 139-147. doi: 10.1016/s0082-0784(69)80398-x

37. Chu, B. and L. Kovásznay, Non-linear interactions in a viscous heat-conducting compressible gas. Journal of Fluid Mechanics, 1958. **3**(5): p. 494-514. doi: 10.1017/S0022112058000148
38. Sutton, G.P. and O. Biblarz, Rocket Propulsion Elements, 2001, New York: John Wiley.
39. Proudman, I., An example of steady laminar flow at large Reynolds number. Journal of Fluid Mechanics, 1960. **9**(4): p. 593-602. doi: 10.1017/S002211206000133X
40. Beddini, R.A., Injection-induced flows in porous-walled ducts. AIAA Journal, 1986. **24**(11): p. 1766-1773. doi: 10.2514/3.9522
41. Chedevergne, F., G. Casalis, and T. Féraille, Biglobal linear stability analysis of the flow induced by wall injection. Physics of Fluids, 2006. **18**(1): p. 014103-014114. doi: 10.1063/1.2160524
42. Griffond, J. and G. Casalis, On the nonparallel stability of the injection induced two-dimensional Taylor flow. Physics of Fluids, 2001. **13**(6): p. 1635-1644. doi: 10.1063/1.1367869
43. Majdalani, J. and T. Saad, The Taylor-Culick profile with arbitrary headwall injection. Physics of Fluids, 2007. **19**(9): p. 093601-093610. doi: 10.1063/1.2746003
44. Majdalani, J., Analytical Models for Hybrid Rockets, in Fundamentals of Hybrid Rocket Combustion and Propulsion, K. Kuo and M.J. Chiaverini, Editors. 2007, AIAA Progress in Astronautics and Aeronautics: Washington, DC. p. 207-246.
45. Munson, B.R., D.F. Young, and T.H. Okiishi, Fundamentals of Fluid Mechanics. Fourth edition, 2002: John Wiley & Sons, Inc.
46. Anderson, J.D., Modern Compressible Flow with Historical Perspective. 3rd edition, 2003, New York: McGraw-Hill.
47. Carrier, B.T. and F.D. Carlson, On the propagation of small disturbances in a moving compressible fluid. Quarterly of Applied Mathematics, 1946. **4**(1): p. 1-12. doi:
48. Arfken, G.B. and H.-J. Weber, Mathematical methods for physicists. Sixth edition, 2005: Elsevier. 1182.
49. Majdalani, J., Improved Flowfield Models in Rocket Motors and the Stokes Layer with Sidewall Injection, in Department of Mechanical Engineering1995, University of Utah: Salt Lake City, UT.

50. Richardson, E., The amplitude of sound waves in resonators. Proceedings of the Physical Society, London, 1928. **40**(27): p. 206-220. doi: 10.1088/0959-5309/40/1/328
51. Halliday, D., R. Resnick, and J. Walker, Fundamentals of Physics. 9th edition, 2011.
52. Fischbach, S.R., Streaming Effects in Liquid Injection Rocket Engines with Transverse Mode Oscillations, in Department of Aerospace Engineering2007, University of Tennessee: Knoxville, TN.
53. French, J.C. and G.A. Flandro. Linked solid rocket motor combustion stability and internal ballistics analysis. in AIAA. 2005. Fort Lauderdale, FL.

Appendix A

Standing Vortical Wave

A. Travelling vs. Standing Waves

A travelling wave propagates throughout a medium, i.e. it is a wave whose nodes and extrema move in the direction of propagation [51]. Sinusoidal planar waves travelling in the positive and negative z-directions would have the following forms, respectively:

$$u(z,t) = A\sin(kz - \omega t) \tag{A.1}$$

$$u(z,t) = A\sin(-kz - \omega t) \tag{A.2}$$

where A is the amplitude of the travelling waves.

In one dimension, a standing wave is produced when two waves with the same frequency, wavelength and amplitude are combined while travelling in opposite directions. The resulting stationary wave's nodes and extrema do not propagate throughout the medium, hence the term standing [51]. The resulting wave is the sum of the two travelling waves:

$$u_S(z,t) = A\sin(kz - \omega t) + A\sin(-kz - \omega t) = 2A\sin(-\omega t)\cos(kz) \tag{A.3}$$

The linear superposition of travelling or standing waves forms wave packets. These groups of waves are characterized by the group velocity which represents the propagation speed of the packet in a medium. The group velocity is defined as:

$$V_{group} \equiv \frac{\partial \omega}{\partial k} \tag{A.4}$$

where ω is the wave's angular frequency and k is the angular wavenumber. In contrast, the propagation velocity of a single wave is known as phase velocity. In addition to linear superpostion, it is possible to add different waves nonlinearly. The result is a steepened wave that is discussed in Appendix B.

B. Standing Vorticoacoustic Wave

As shown in Eq. (5.24), the formulated vortical wave is a right-travelling wave. Since the flow is choked at the nozzle, the chamber's exit acts as a solid boundary that causes the wave to bounce back [52]. The left-travelling reflected wave exhibits the form

$$\tilde{u}_r = G(r,\theta,z)\exp\left[i\left(-\frac{S}{F}z - k_{mn}t\right)\right] \tag{A.5}$$

Summing Eqs. (5.24) and (A.5) yields the standing radial vortical wave:

$$\tilde{u}_r = 2G(r,\theta,z)e^{-ik_{mn}t}\cos\left(\frac{S}{F}z\right) \tag{A.6}$$

which, in our problem, becomes

$$\tilde{u}_r = \frac{2A_r i}{k_{mn}\gamma}e^{-ik_{mn}t}J'_m(k_{mn}r)\cos(m\theta)\cos\left(\frac{S}{F}z\right)\exp\left(-\frac{z}{S_p F^2}\right) \tag{A.7}$$

where A_r is the integration constant first introduced in Eq. (4.54). To ensure the satisfaction of the no-slip boundary condition at the headwall $\left(u'(z=0)=0\right)$, it can be shown that A_r must be equal to $-1/2$. The resulting vorticoacoustic standing wave in the radial direction can be expressed as

$$u_r' = \frac{i}{k_{mn}\gamma} e^{-ik_{mn}t} J_m'\left(k_{mn}r\right)\cos\left(m\theta\right)\left[1-\cos\left(\frac{S}{F}z\right)\exp\left(-\frac{z}{S_p F^2}\right)\right] \tag{A.8}$$

in the radial direction and

$$u_\theta' = \frac{i}{k_{mn}\gamma}\frac{m}{r} e^{-ik_{mn}t} J_m\left(k_{mn}r\right)\sin\left(m\theta\right)\left[1-\cos\left(\frac{S}{F}z\right)\exp\left(-\frac{z}{S_p F^2}\right)\right] \tag{A.9}$$

in the tangential direction. The axial vortical velocity component is not addressed in this appendix since it has been shown that it is an order smaller than the dominating transverse waves, and is thus beyond the scope of this study.

Figures 14 and 15 are used to display the mode shapes of the radial and tangential disturbances corresponding to the standing wave along the axis of the chamber at varying times. In order to be consistent with the plots corresponding to the travelling wave, results are depicted for $\delta = 0.000647$, $r = 1/\sqrt{2}$, $\theta = \frac{1}{4}\pi$, the first tangential/radial modes using k_{11} and different Mach numbers $\left(M_b = 0.3, 0.03 \,\&\, 0.003\right)$. The plots in Fig. 14 span over half a cycle, thus showcasing the behavior of the standing wave with respect to time. The most striking result is the maximum value of the standing wave when compared to its travelling counterpart. For all cases, the standing wave exhibits peaks that are twice as large as those of the corresponding travelling wave. This analysis demonstrates the importance of accounting for the reflected waves in a chamber.

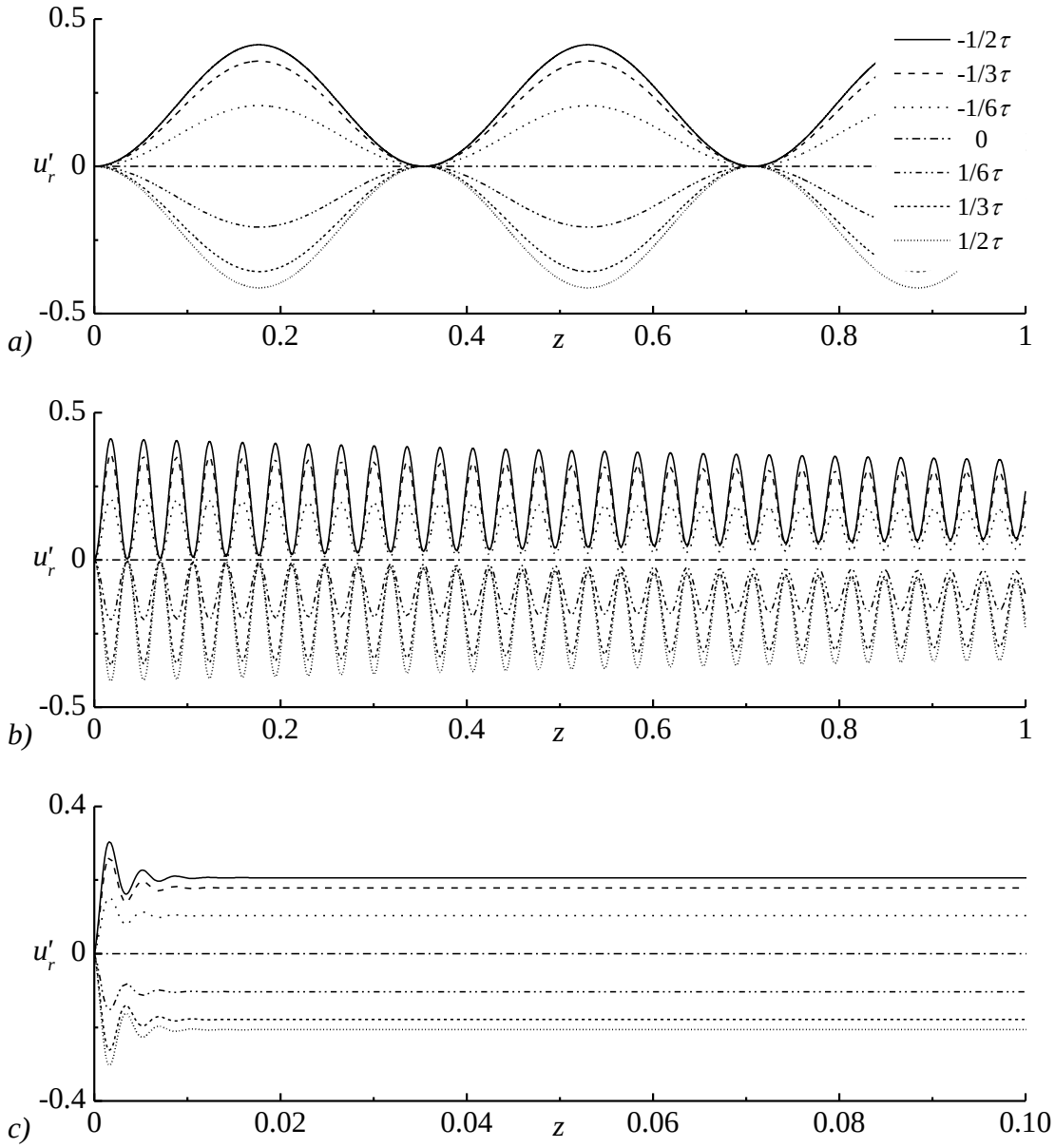

Figure 14. Unsteady vorticoacoustic velocity for the radial standing wave at inlet Mach numbers corresponding to: a) 0.3, b) 0.03 and c) 0.003.

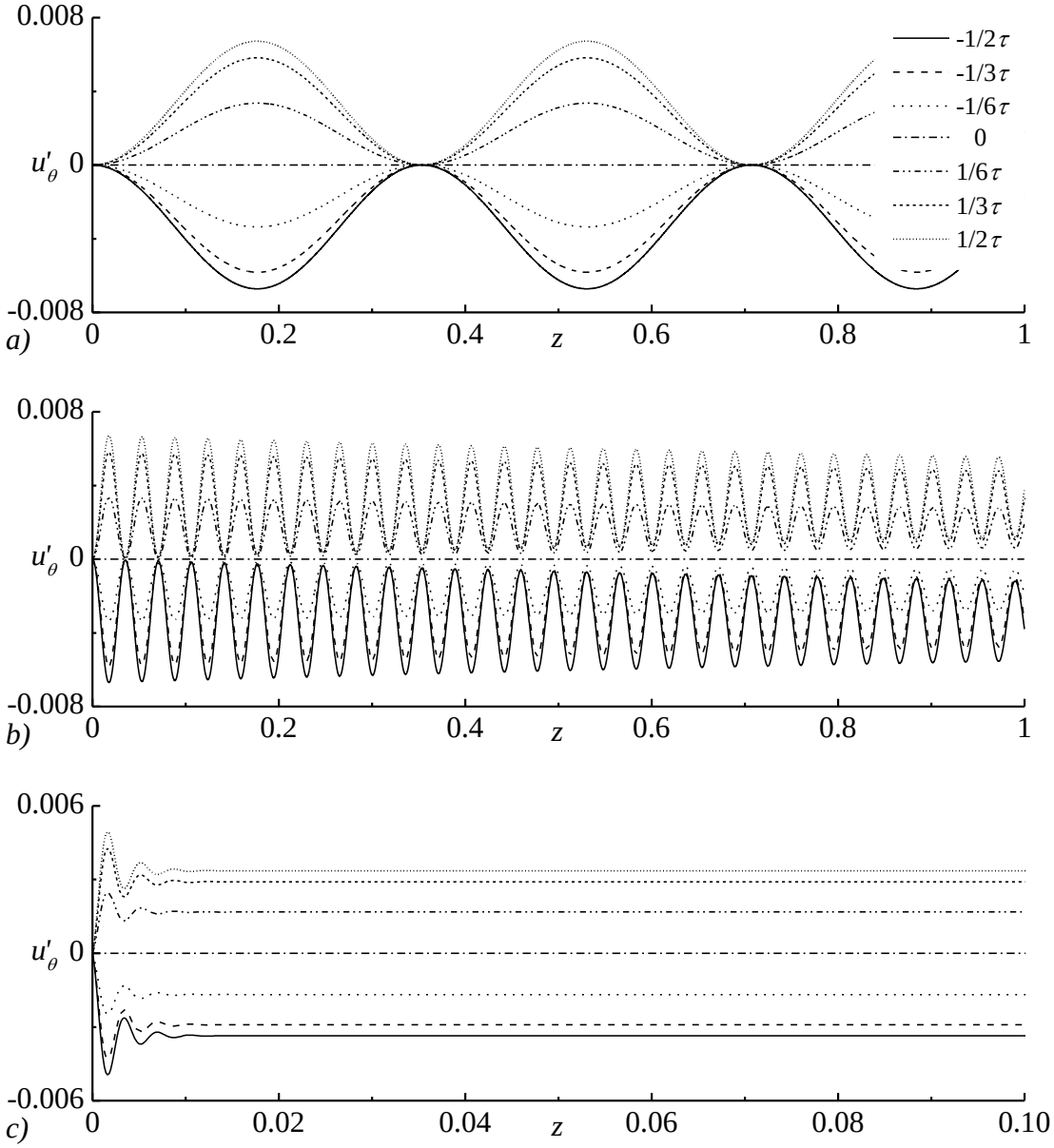

Figure 15. Unsteady vorticoacoustic velocity for the tangential standing wave at inlet Mach numbers corresponding to: a) 0.3, b) 0.03 and c) 0.003.

Appendix B

Wave Steepening

Wave steepening is a phenomenon that refers to a shock-like behavior of waves. Steepening can affect strong sound waves propagating in gas, due to the dependency on temperature and pressure. The presence of strong waves heats the gases near each pressure front, thus increasing the local speed of sound. This change leads to high pressure fronts outrunning pressure troughs, thus resulting in shock-like motion due to non-linear steepening [46].

Similarly, the vorticoacoustic waves present in a LRE chamber can couple in linear and non-linear fashions to produce steepened waves. The resulting steepened waves are dreaded because of their shock-like behavior in the chamber and the concentration of pressure and velocity peaks. In a recent study on the subject [53], waves were shown to steepen in the longitudinal, radial and tangential directions. In this section, the steepening of standing waves in the tangential direction is revisited and extended to include the corresponding velocities. The steepened pressure can be expressed in terms of the normalized variables as:

$$p'(r,\theta,t) = \sum_{m} \frac{1}{m} e^{-imk_{1n}t} J_m(k_{mn} r) \cos(m\theta) \tag{B.1}$$

Similarly, the steepened vorticoacoustic velocities can be deduced via Eqs. (A.8) and (A.9) to the extent of producing:

$$u_r'(r,\theta,z,t)=\sum_m \frac{1}{m}\frac{i}{k_{mn}\gamma}e^{-imk_{1n}t}J_m'(k_{mn}r)\cos(m\theta)\left[1-\cos\left(\frac{S}{F}z\right)\exp\left(-\frac{z}{S_pF^2}\right)\right] \quad \text{(B.2)}$$

$$u_\theta'(r,\theta,z,t)=\sum_m \frac{i}{k_{mn}\gamma}\frac{1}{r}e^{-imk_{1n}t}J_m(k_{mn}r)\sin(m\theta)\left[1-\cos\left(\frac{S}{F}z\right)\exp\left(-\frac{z}{S_pF^2}\right)\right] \quad \text{(B.3)}$$

Figures 16, 17 and 18 illustrate the travelling tangential shock wave that results from summing the first forty modes. These figures showcase the steepened acoustic pressure and corresponding vorticoacoustic transverse velocities for the zero radial mode $(n=0)$ during half a cycle, namely when the wave front crosses half of the chamber.

In addition to the travelling shockwave, Fig. 16 depicts the pressure nodal line (red). As the steep fronted wave sweeps along the chamber's circumference, its nodal line crosses the centerline. Note that the unsteady pressure vanishes at $r=0$ since the center happens to be a common node for the different mode numbers. Figures 17 and 18 illustrate the vorticoacoustic velocities corresponding to the steepened pressure wave. In regions of increased pressure, higher velocities are expected as shown in these figures.

Furthermore, it should be noted that the steepened wave were obtained by superposing standing vorticoacoustic waves. Previous studies have shown that travelling waves can also steepen and result in pressure fronts spinning around the centerline [53]. Moreover, it should be noted that the summation scheme assumes that the final shape of the motion is similar to a sawtooth wave [53]. Further investigations must be conducted in order to understand the linear and nonlinear mode coupling phenomena that lead to steepened waves in simulated liquid rocket engines.

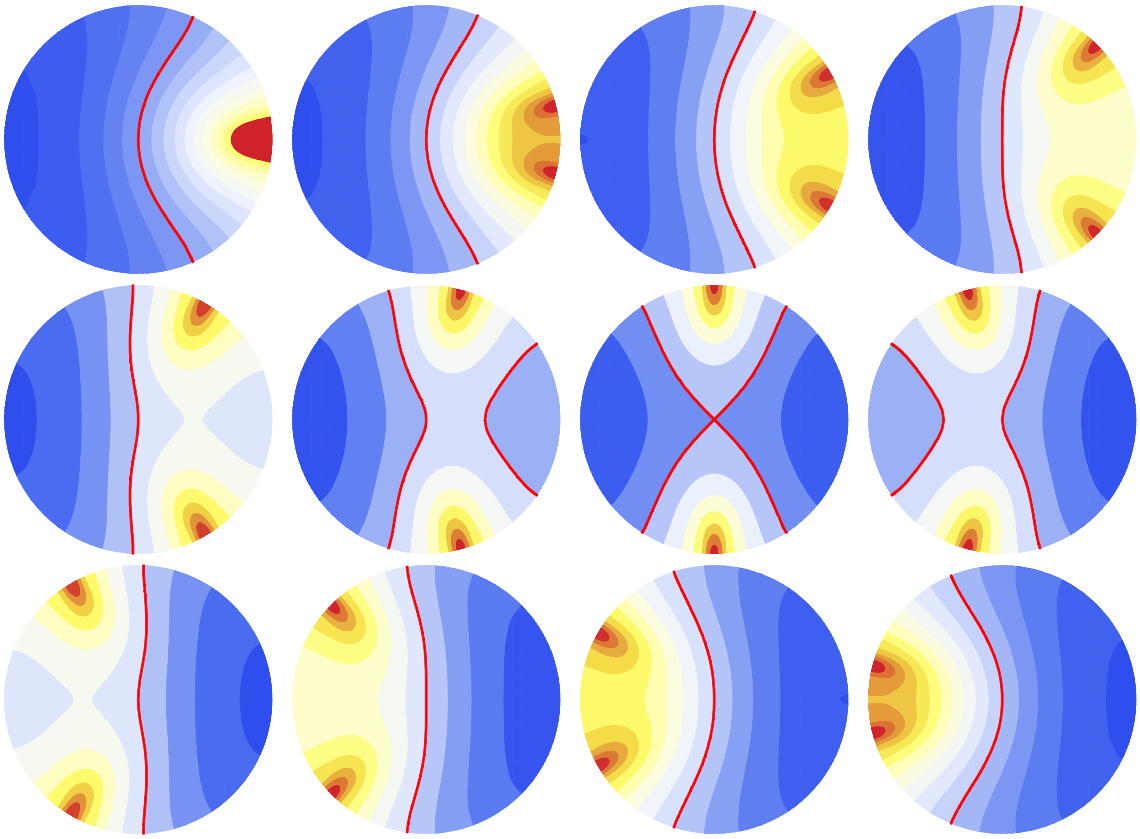

Figure 16. Travelling tangential shock wave due to the steepening of the first forty standing tangential pressure modes.

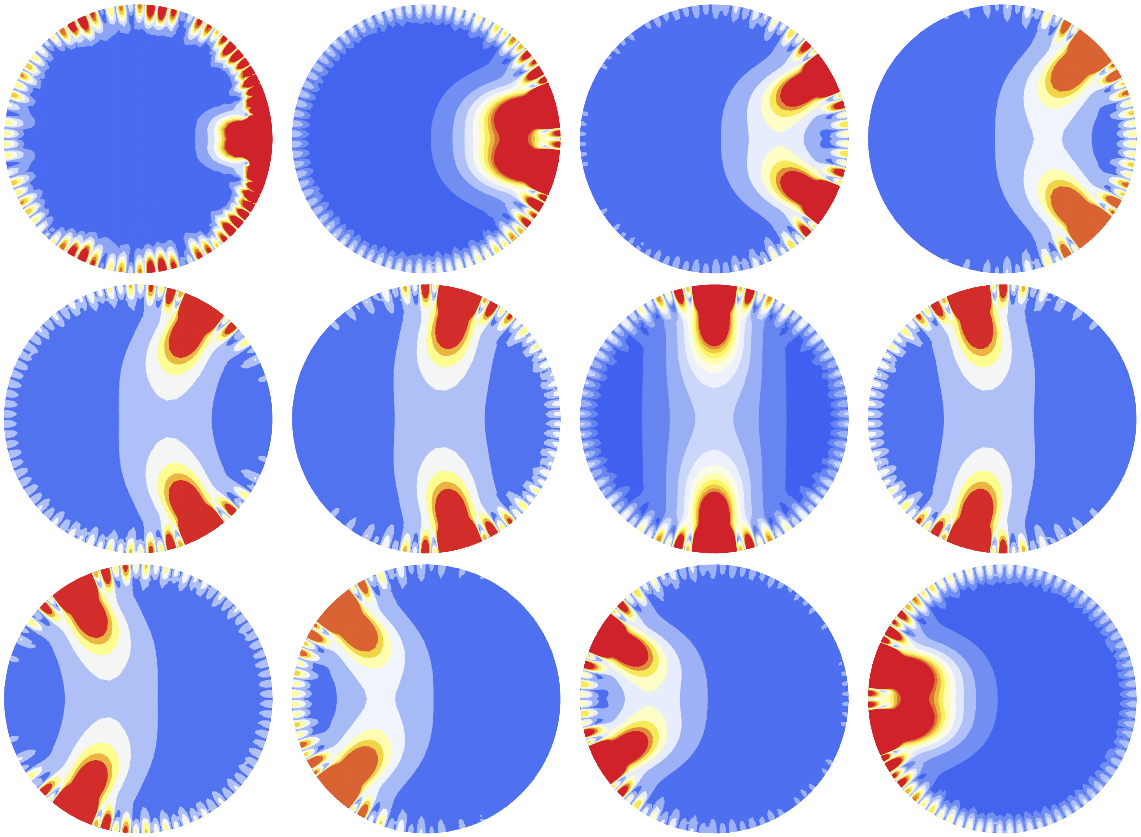

Figure 17. Unsteady vorticoacoustic velocity magnitude corresponding to a travelling tangential shock wave due to the steepening of the first forty standing tangential velocity modes.

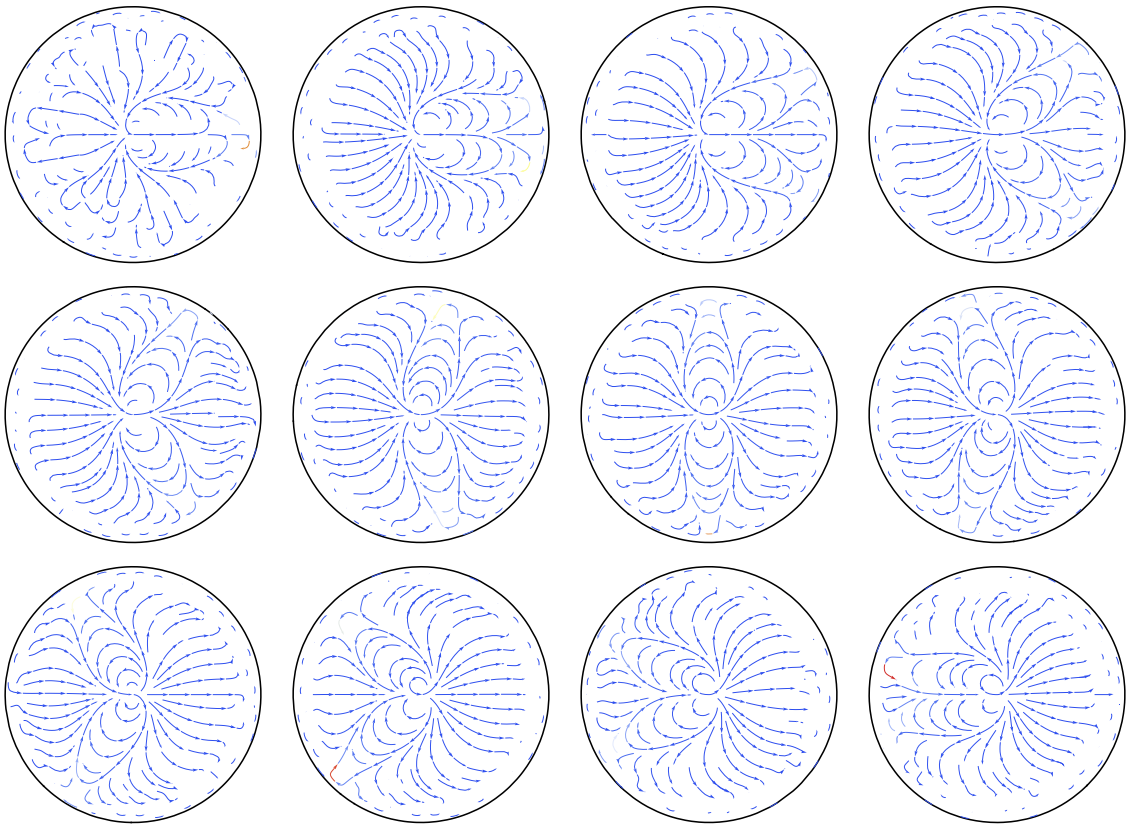

Figure 18. Unsteady vorticoacoustic velocity vectors corresponding to a travelling tangential shock wave due to the steepening of the first forty standing tangential velocity modes.

Vita

Charles Haddad was born in Beirut, Lebanon on December 1, 1987. He graduated as class Valedictorian from Collège Notre Dame de Louaizé. Subsequently, he pursued a Bachelor of Engineering in Mechanical Engineering at Notre Dame University, Lebanon where he graduated *Summa Cum Laude* in Fall 2009 and received the Dean's Award for Academic Excellence. While completing his undergraduate degree, Charles volunteered for ASME where he chaired the student section at NDU, the student district operating board for Middle-East and Africa and various committees and conferences. These activities enabled him to gain and sharpen his leadership and teambuilding skills while developing his talents for multi-national and cultural management. In recognition of his efforts, he was twice the recipient of the Dean's Award for Outstanding Services. At the University of Tennessee Space Institute, Charles joined the Advanced Theoretical Research team, headed by Dr. Joseph Majdalani, where he focused his studies on Fluid Mechanics and Perturbation Methods to complement his research. He will graduate in December 2011 with a Master of Science in Aerospace Engineering.